Improving the selectivity of photocatalytic NO_x abatement through improved O_2 reduction pathways using $Ti_{0.909}W_{0.091}O_2N_x$ semiconductor nanoparticles: from characterization to photocatalytic performance

Andrea Folli, Jonathan Z. Bloh, Katherine Armstrong, Emma Richards, Damien M. Murphy, Li Lu, Christopher J. Kiely, David J. Morgan, Ronald I. Smith, Abbie C. Mclaughlin and Donald E. Macphee

Published version information

Citation: A Folli et al. "Improving the selectivity of photocatalytic NO_x abatement through improved O_2 reduction pathways using $Ti_{0.909}W_{0.091}O_2N_x$ semiconductor nanoparticles: from characterization to photocatalytic performance." ACS Catalysis vol. 8 (2018): 6927-6938.

DOI: 10.1021/acscatal.8b00521

Improving the selectivity of photocatalytic NOx abatement through improved O_2 reduction pathways using $Ti_{0.909}W_{0.091}O_2N_x$ semiconductor nanoparticles: from characterisation to photocatalytic performance

Andrea Folli,*,† Jonathan Z. Bloh,‡ Katherine Armstrong,† Emma Richards,† Damien M. Murphy,† Li Lu,¶ Christopher J. Kiely,¶,† David J. Morgan,† Ronald I. Smith,§ Abbie C. Mclaughlin,‖ and Donald E. Macphee‖

†*School of Chemistry, Cardiff University, Main Building, Park Place, Cardiff CF10 3AT, UK.*

‡*DECHEMA Research Institute, Theodor-Heuss-Allee 25, Frankfurt am Main 60468, Germany.*

¶*Department of Materials Science and Engineering, Lehigh University, Whitaker Laboratory, 5 East Packer Ave, Bethlehem, PA 18015, USA.*

§*ISIS Neutron and Muon Source, STFC Rutherford Appleton Laboratory, Harwell Campus, Didcot OX11 0QX, UK.*

‖*Department of Chemistry, University of Aberdeen, Meston Building, Meston Walk, Aberdeen AB24 3UE, UK.*

E-mail: follia@cardiff.ac.uk

Abstract

In this paper we provide detailed insight into the electronic-crystallographic-structural relationship for $Ti_{0.909}W_{0.091}O_2N_x$ semiconductor nanoparticles, explaining the mutual electronic and magnetic influence of the photo-induced, stable N- and W-based paramagnetic centres, their involvement in the photo-induced charge carriers trapping and their role in improving the nitrate selectivity of the photocatalytic oxidation of NOx to nitrates. In particular, reduced tungsten species in various crystallographic environments within the anatase host lattice were observed to play a fundamental role in storing and stabilising photo-generated electrons. Here we show how these reduced centres can catalyse multi-electron transfer events without the need for rare and expensive platinum group metals (PGMs). This allows for a versatile and elegant design of redox potentials. As a result, electron transfer processes that are kinetically inaccessible with metal oxides such as TiO_2 can now be accessed, enabling dramatic improvements in reaction selectivity. The photocatalytic abatement of NOx towards non-toxic products is exemplified here and is shown to pivot on multiple routes for molecular oxygen reduction. The same rationale can furthermore be applied to other photocatalytic processes. The observations described in this work could open new exciting avenues in semiconductor photocatalysis for environmental remediation technologies, where the optimisation of molecular oxygen reduction, together with the pollutant species to be oxidised, becomes a central element of the catalyst design, without relying on the use of rare and expensive PGMs.

KEYWORDS: Photocatalysis, nitrate, nitric oxide, nitrogen dioxide, visible light, ORR, EPR.

1 Introduction

Since the first reports of photocatalytic water splitting were published in the 1970s,[1] semiconductor photocatalysis has attracted increasing interest for wastewater remediation,[2–5]

removal of air pollutants,[5–13] self-cleaning surfaces[3,4,11,14] and solar fuels.[1,5,15–22] Much less use of this technology was made in synthetic chemistry as semiconductor photocatalysis is very often non-selective (TiO_2 being, by far, the most used photocatalyst). Furthermore, for the many applications that, in the absence of artificial light sources, are reliant on the Sun for irradiation, photocatalysis only works during the daytime when sufficient sunlight intensity is present (seasons and latitude also play a major role[23]). For environmental remediation applications, the persistance of toxic pollutants due to the temporary unavailability of the remediation technology can cause severe problems for the environment or people's health. Photocatalysts consisting of TiO_2-WO_3 mixed oxides and TiO_2-WO_3 heterojunction films where electron storage and slow electron discharge in the absence of irradiation allow sustained photocatalytic activity in the darkness, have been reported by a few research groups[24–30] and also tested for anticorrosion[25] or VOC removal applications.[27] The common understanding is that photo-generated electrons can be stored in WO_3 due to a typical tungsten bronze chemistry mediated by proton intercalation,[25] and is supported by clear electrochemical evidence.[25] Very recently however, Sotelo-Vazquez et al.[30] observed an unusual electron transfer process in WO_3-TiO_2 heterojunction films composed of vertically aligned nanostructured WO_3 nanorods coated with a conformal layer of TiO_2, in which photo-generated electrons would move from the WO_3 layer into TiO_2. Despite the great interest for these mixed oxides as systems where charge recombination processes are inhibited resulting in performance enhancements beyond the individual components, a structural "picture" of the reduced centres associated with the electron transfer and trapping is often missing.

Here we show that reduced W centres can be used to rationally design multiple routes for molecular oxygen reduction, leading to a significant improvement of selectivity in photocatalysis, exemplified in this work by the NOx oxidation to nitrate. The same rationale can furthermore be applied to other oxide photocatalysts. Using $Ti_{0.909}W_{0.091}O_2N_x$ semiconducting nanoparticles, we provide an in-depth account of the electronic-structural relationship

of their stable W paramagnetic reduced centres, whether associated with isolated W atoms substituting for Ti in the TiO_2 lattice or in surface localised Magneli phase-like W clusters; their magnetic influence on the spin density associated with N-doping; the overall photochemical response and their involvement in the photocatalytic DeNOx process, showing how the W species may influence the selectivity of the oxidation of NO to NO_3^-.

2 Results and Discussion

2.1 Characterisation

Representative high resolution neutron diffraction (154° 2θ detector bank) pattern is shown in Figure 1 and Table 1, for a sample containing 9.1 at.% of W. The Rietveld refinement fit[31] showed that this material is single phase and crystallises with the anatase $I4_1/amd$ space group and has the formula $Ti_{0.909}W_{0.091}O_2$, indicating 9.1 at.% substitution of W for Ti. Other materials synthesised with different amounts of W higher than 0.15 at.%, were also found to crystallise with the same anatase $I4_1/amd$ space group.[32] The lack of peak splitting or superstructure peaks would exclude a change in symmetry upon substituting W for Ti, Figure 2. Rietveld refinement of the model did not show any evidence for an increase in the fractional occupancy of the bulk oxygen (i.e., the oxygen fractional occupancy was refined to within ±1% of the full occupancy and fixed at 1.0). Therefore the *average* bulk oxygen molar content is 2 although this may be different locally within the structure and is likely to be different at the surface. Structural refinement of the neutron diffraction data also showed no evidence of bulk nitrogen, either at the oxygen positions or at interstitial sites.

X-Ray Photoelectron Spectroscopy (XPS) spectra are presented in Figure 3a-d for the O(1s), Ti(2p), N(1s) and W(4d) core-levels respectively; the W(4d) region was analysed over the more common W(4f) region due to the overlap of the W(4f) and Ti(3p) core-levels. Spectra were calibrated to the C(1s) signal at 284.8 eV. Fitting of the O(1s) core-level

spectra (Figure 3a) reveals the presence of lattice Ti-O, 530.3 eV,[33] with shoulders at 531.0 and 532.6 eV, indictive of surface hydroxide[34,35] and carbonate respectively (arising from the handling of samples in air). The Ti $2p_{3/2}$ and $2p_{1/2}$ peaks at 459.0 eV and 465.0 eV respectively (doublet separation of about 6 eV) together with the satellite peak at 472.5 eV shifted by about 13.5 eV from the main Ti $2p_{3/2}$ peak (Figure 3b), are typical of Ti(IV) in TiO_2.[36] Comparison of the corrected oxygen and titanium core levels give a O/Ti ratio of 1.97. The N(1s) region (Figure 3c) clearly reveals two species, with binding energies of 400.2 eV and 401.9 eV. The lower binding energy species can be attributed to surface NH_x species, likely to remain from the synthesis procedure where $(NH_4)_6H_2W_{12}O_{40} \cdot xH_2O$ served as a source for both N and W dopants, whereas the higher binding energy species is attributed to N-O bonds,[37] the photochemistry of which will be discussed later through a combination of UV-vis diffuse reflectance spectroscopy and electron paramagnetic resonance (EPR) spectroscopy. No peaks at 396.0 to 397.0 eV indicative of substitutional N doping[37] were observed. Quantification of the N doping by XPS gave a total N content of 0.38 at.%. The fact that N was detected by XPS and not by neutron diffraction could be explained with N being present almost entirely in the surface region of the nanoparticles.

Observation of W $4d_{5/2}$ peak at 247.5 eV and $4d_{3/2}$ peak 260.0 eV are indicative of W(VI) oxidation state; however, lower binding energy shoulders are noted at 241.8 eV and 254.3 eV respectively (arrows in Figure 3d), both shifted by exactly 5.7 eV from their main peaks, and are evidence of W in a reduced state. Further explanation of these reduced W species will be provided by EPR spectroscopy. XPS quantification for W showed a total W content of 3.9 at.% with ca. 6 % of the total W content present in the reduced state. The discrepancy of the total W content measured by XPS from that of 9.1 at.% indicated by neutron diffraction is attributed to a low dispersion or larger W-containing clusters at the nanoparticle surface, resulting in an apparent decrease in the surface concentration detectable by XPS. To further verify the overall amount of W in the nanoparticles, we performed elemental analysis which gave a total mass content of 20 to 25 % of equivalent WO_3, corresponding to a loading of 8.3

to 10.4 at.%, confirming the 9.1 at.% aimed during the synthesis and therefore the presence of larger W-containing clusters at the nanoparticle surface.

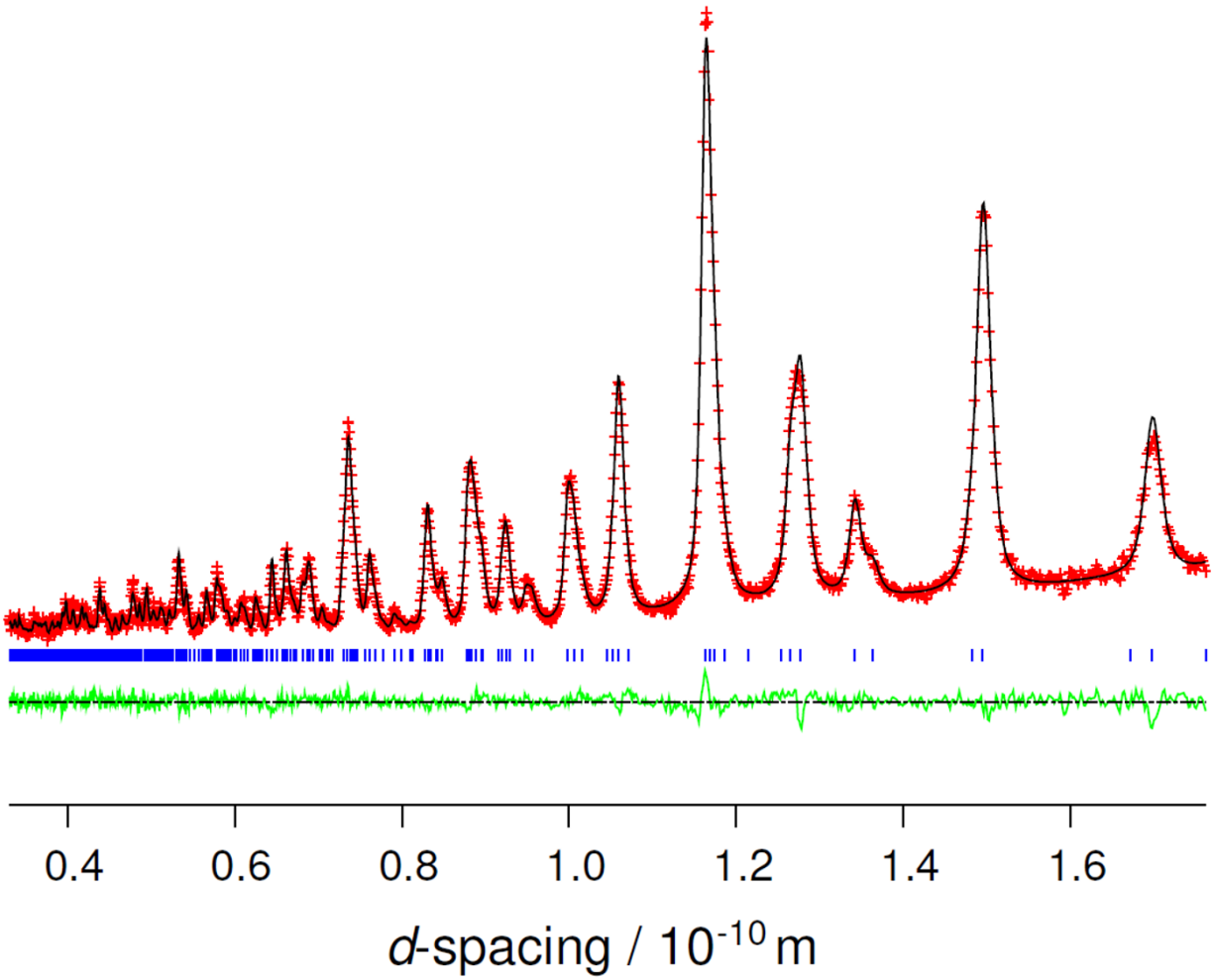

Figure 1: Fitted powder neutron diffraction pattern collected at 303 K from $Ti_{0.909}W_{0.091}O_2N_x$ in the GEM backscattering detector bank (average $2\theta = 154°$). The figure shows the Rietveld fit (red +) to the experimental pattern (black trace), the theoretical reflection positions (small blue vertical lines) and the residual (obs-calc) profile (green trace).

Representative high angle annular dark field (HAADF) aberration corrected scanning transmission electron microscope (STEM) images of the $Ti_{0.909}W_{0.091}O_2N_x$ sample are shown in Figure 4a and b, in which the W component is readily visible via the mass contrast afforded by this technique. W has a tendency to incorporate substitutionally into the Ti cation sub-lattice sites, in good agreement with the neutron diffraction results. At this high concentration however, W also forms discrete clusters on the surface of the nanoparticles

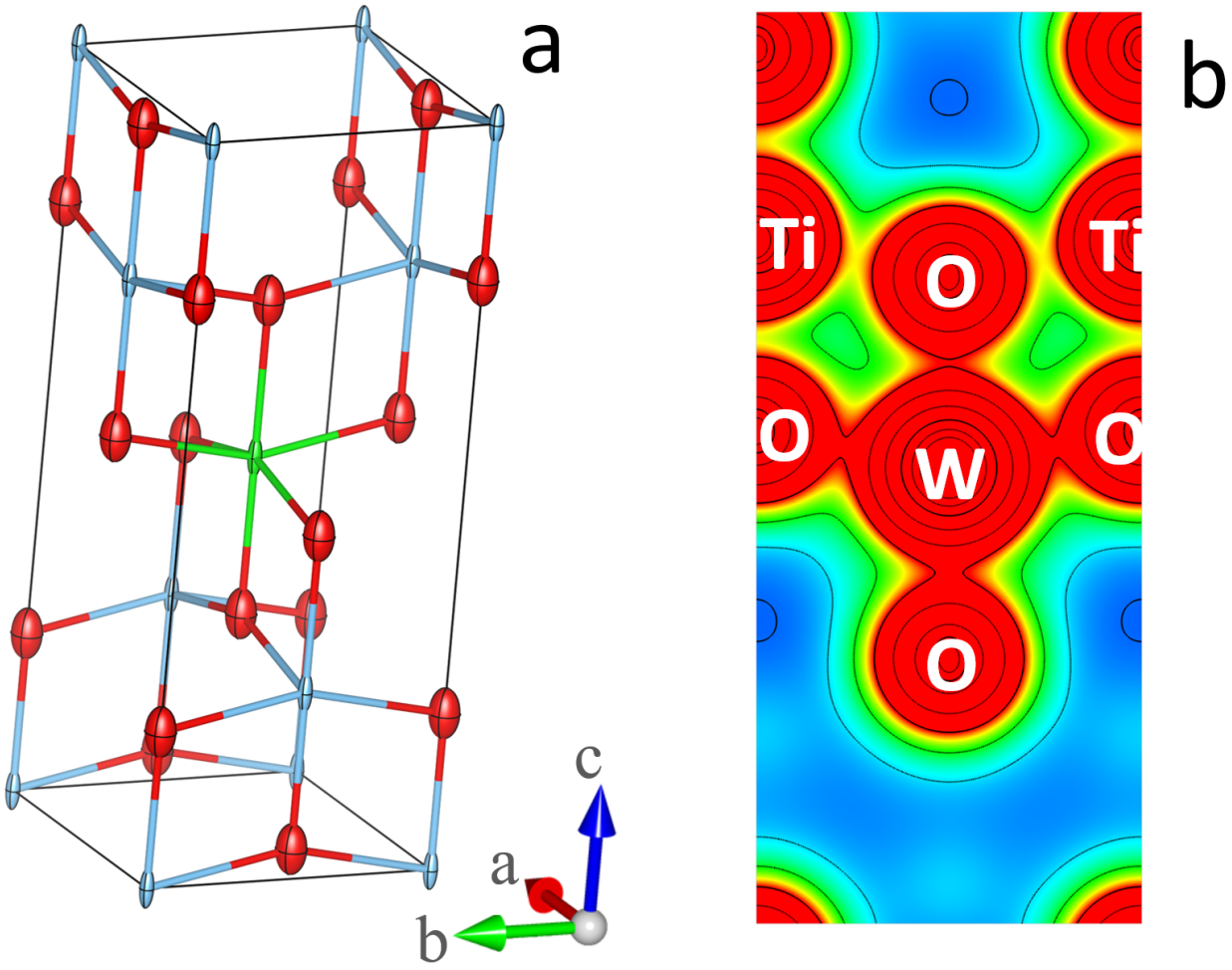

Figure 2: (a) Representation of a W substitution of a Ti site in an anatase unit cell based on the neutron diffraction refined parameters in Table 1. In $Ti_{0.909}W_{0.091}O_2N_x$ nanoparticles, W substitution occurs, on average, once per 2.74 unit cells. Lattice Ti and O are shown in blue and red respectively. The substitutional W ion is shown in green. (b) Electron density distribution for a W substitution determined by Maximum Entropy Method (MEM) based pattern fitting from neutron powder diffraction data at a resolution of $0.02a_0^{-1}$ and drawn as cumulative [1 0 0] planes between 0.25a and 0.75a, using as a centre of projection x=0, y=z=0.5. MEM electron density bulk contours were drawn using a $F(N) = AB^{N/step}$ function, with $A = 1$, $B = 10$, $step = 3$, between $N_{min} = -2$ and $N_{max} = +2$. The plot shows the greater polarising power of the substitutional W^{6+} ions on the O^{2-} electron density when compared to Ti^{4+}. The 2D plot was obtained using the VESTA visualisation software for electronic and structural analysis.[38]

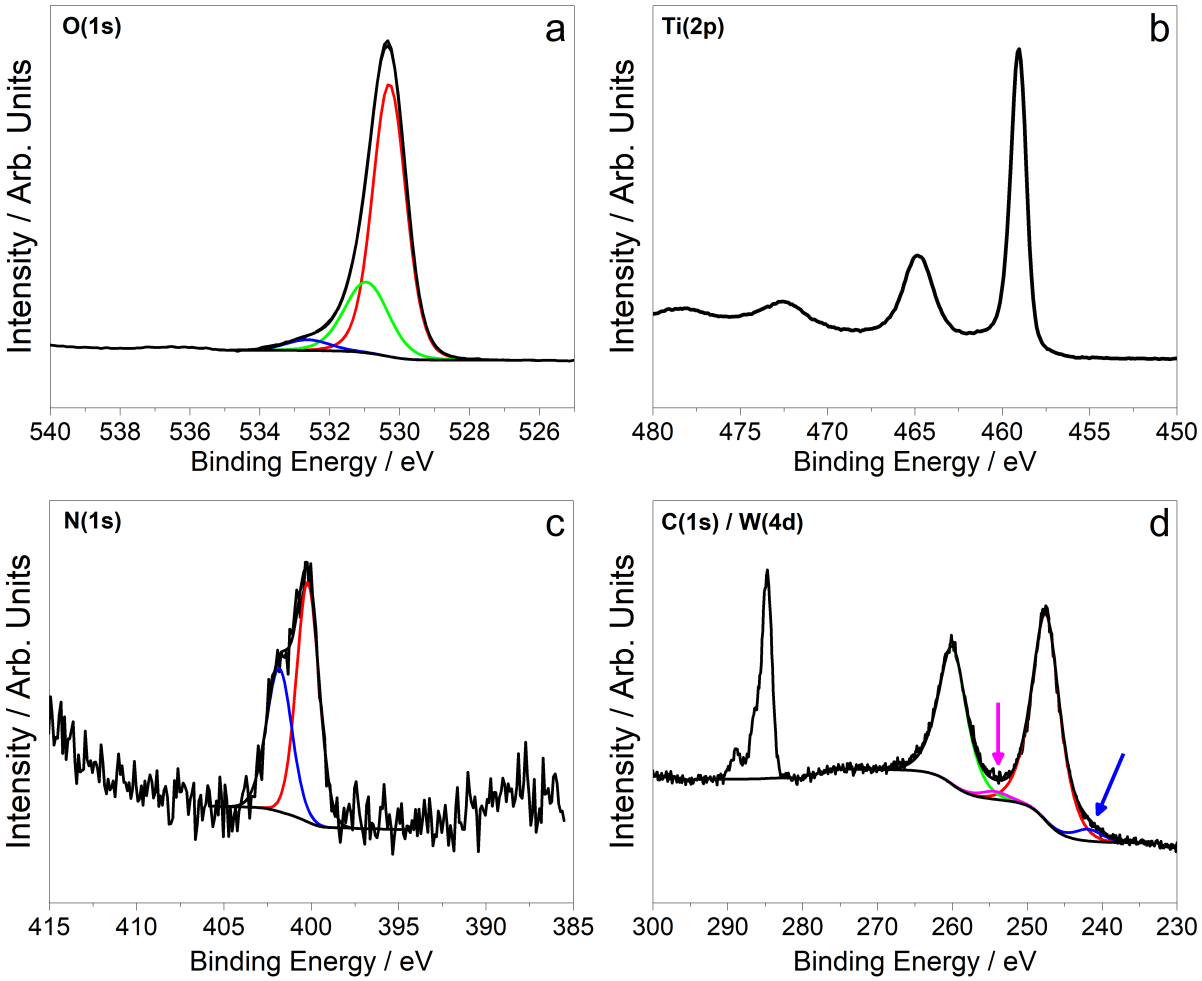

Figure 3: XPS spectra of the (a) O(1s), (b) Ti(2p), (c) N(1s) and (d) W(4d) core-levels for $Ti_{0.909}W_{0.091}O_2N_x$ nanoparticles. Spectra were charge corrected to the C(1s) peak at 284.8 eV.

Table 1: Refined structural parameters for $Ti_{0.909}W_{0.091}O_2N_x$ in the space group $I4_1/amd$ from neutron diffraction data.

a=b / Å	c / Å	Volume / Å^3	R_{wp} / %	R_p / %	χ^2 -		
3.7899(1)	9.4801(5)	136.16(2)	2.45	2.12	1.47		
Atom -	Wyckoff site -	Occupancy -	x -	y -	z -	U_{11}=U_{22} / Å^2	U_{33} / Å^2
Ti	4*b*	0.909(2)	0.0	0.25	0.375	0.0006(4)	0.0053(6)
W	4*b*	0.091(2)	0.0	0.25	0.375	0.0006(4)	0.0053(6)
O	8*e*	1.0	0.0	0.25	0.16522(6)	0.0032(3)	0.0088(3)

(bright areas in Figure 4b), corroborating the results from our XPS spectroscopy for this sample. These clusters are not crystalline WO_3.

The diffuse reflectance UV-vis spectrum (Figure 5a) of the $Ti_{0.909}W_{0.091}O_2N_x$ sample exhibits the typical profile corresponding to the band-gap transition of anatase overlapped with an edge in the visible field from 400 to 550 nm. The absorption edge of undoped anatase is included for reference (Figure 5a). The corresponding Tauc plot (in the form useful for indirect band gap semiconductors) for the $Ti_{0.909}W_{0.091}O_2N_x$ sample (Figure 5b) shows that the portion of the optical absorption profile in the UV corresponds to an optical band gap of 3.17 ± 0.01 eV. This can be attributed to the electronic transition (Ti 3d $\leftarrow$ O 2p) of anatase and represents the intrinsic band gap of the semiconductor. The portion of the absorption edge in the visible field corresponds to a photon energy of 2.38 ± 0.02 eV, attributable to an electronic transition from an intraband gap state, due to the presence of interstitial N doping[37,39] to the CB. This is responsible for the pale yellow colour of the sample. In the case of undoped anatase, the optical absorption profile in the UV corresponds to an optical band gap of 3.27 ± 0.03 eV, without any other optical absorption features, as

expected. The full band structure determination, obtained by optical spectroscopic methods plus electrochemical impedance spectroscopy and Mott-Schottky analysis, was reported in one of our recent works[32] to which the reader should refer.

N_2 adsorption isotherms (not reported here) and subsequent BET analysis on the $Ti_{0.909}W_{0.091}O_2N_x$ sample, revealed a specific surface area of $86.9\,m^2\,g^{-1}$ corresponding to a primary particle size of about 20 nm, in line with Rietveld refinement results of 20 to 30 nm (from the observed broadened peak profiles).

Analysis and simulation of the continuous wave (CW) EPR spectra in the free spin region, i.e. $g \approx 2.0$ (Figure 6) revealed the presence of three distinctive N-O paramagnetic centres, deconvoluted in the figure as signals N1, N2 and N3 respectively. The centre N1 can be attributed to the paramagnetic molecule of nitric oxide, NO,[37,40] showing the typical spectrum of an 11 electrons π radical in the adsorbed form, characterised by: i. an anisotropic EPR profile with $g_x \approx g_y \approx 2.0$ and $g_z < 2.0$ (Table 2) and ii. anisotropic hyperfine structure arising from the coupling of the unpaired electron with the non-zero nuclear spin ^{14}N nucleus (natural abundance 99.63 % and $I(^{14}N)$=1 hence signal multiplicity $2I$+1=3) (Table 2). The EPR spectrum of NO in the gas phase is generally not observable in the free spin region; however, it becomes visible when the molecule is weakly adsorbed and polarized on a cationic surface centre at T <170 K.[41] The fact that the EPR profile is present after each sample was evacuated for at least 12 hours at 393 K and under dynamic vacuum, ca. 10^{-4} bar, signifies that this NO is not adsorbed on the exposed surface of the sample, rather it is encapsulated in bulk and sub-surface microvoids (or closed pores) generated during the synthetic process, as proved by previous studies on similar systems.[40] The paramagnetic center N2 consists of an interstitial N chemically bound to a lattice O ion forming a $N_iO^\bullet$ group[42] carrying one electron in the π^* antibonding[37] singly occupied molecular orbital (SOMO). $N_iO^\bullet$ is effectively an intraband gap NO^{2-} state also exhibiting an anisotropic EPR profile. g- and A-values are listed in Table 2. Finally, N3 is again a $N_iO^\bullet$ group similar to N2 but influenced by a close-range interaction with a lattice W^{6+} ion. Within this W-O-N close-range arrangement, the

highly polarising W^{6+} ion pulls electron density away from the lattice oxygen, which in turn causes an increase in the N 2p character of the π^* antibonding SOMO of the $N_iO^\bullet$ unit. In other words, the spin density associated with the unpaired electron is more localised on the N atom when compared to the case of the N2 centre.[43] As a result, the g-values decrease (smaller g_{iso}) and A-values increase (greater a_{iso}) in comparison to the N2 centre (Table 2). The EPR signal of the N3 centre is also characterised by super-hyperfine splitting (Table 2) arising from magnetic interaction with the ^{183}W nucleus (natural abundance 14.31 % and $I(^{183}W)=1/2$). N1 and N2 centres are well known and characterised[32,37,40,42–46] while N3 was first reported in one of our previous works[43] and was here confirmed. EPR signals associated with the reduced W species detected in our XPS spectra were observable at much larger magnetic field positions (Figure 7). The g-values (Table 3) match previously reported EPR signals of W^{5+} species in different surface crystallographic environments.[47–49] The signal W1 can be associated with coordinatively unsaturated W^{5+} species in W_xO_y clusters strongly anchored to the surface of the host crystal whilst W2 corresponds to W^{5+} in tungsten bronze-like superstructures, weakly bound to the surface of the host crystal. This is in line with the presence of surface clusters identified by our HAADF aberration corrected-STEM (Figure 4). The very low g-values are expected given: i. the very large spin-orbit coupling in the 5d orbitals of W^{5+} (ζ=2700 cm^{-1})[50] which causes a large variation from the free spin g-value of 2.0023 (i.e. the unpaired electron is highly "bound" to its nucleus), and ii. W^{5+} is a d^1 ion (ions with a number of d electrons < 5 exhibit negative variation of the g-values from free spin). EPR investigation was inconclusive as for the presence of W^{4+} and/or W^{3+} high spin states in the as-synthesised nanoparticles.

.

.

.

.

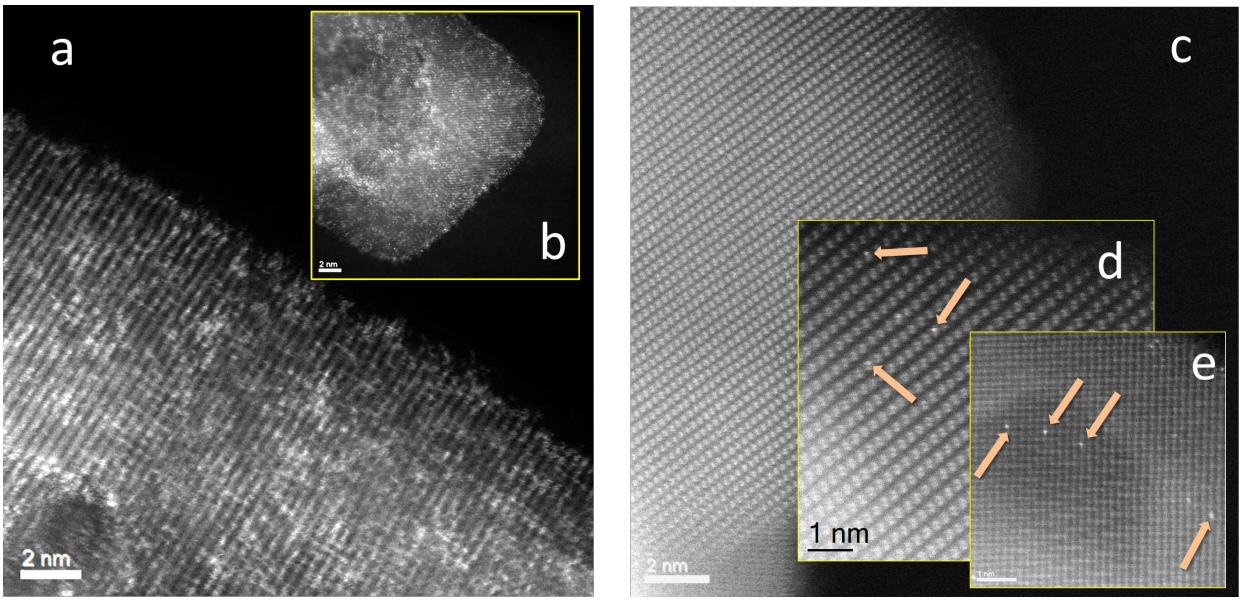

Figure 4: (a), (b) Representative high angle annular dark field (HAADF)-STEM images of $Ti_{0.909}W_{0.091}O_2N_x$. The presence of both substitutional W and W-containing surface clusters are evident in the images. A comparison is made with (c), (d) and (e) showing high angle annular dark field (HAADF)-STEM images of a sample with much lower W content, i.e. $Ti_{0.999}W_{0.001}O_2N_x$, where only substitutional W (arrows indicating brighter spots) is present.

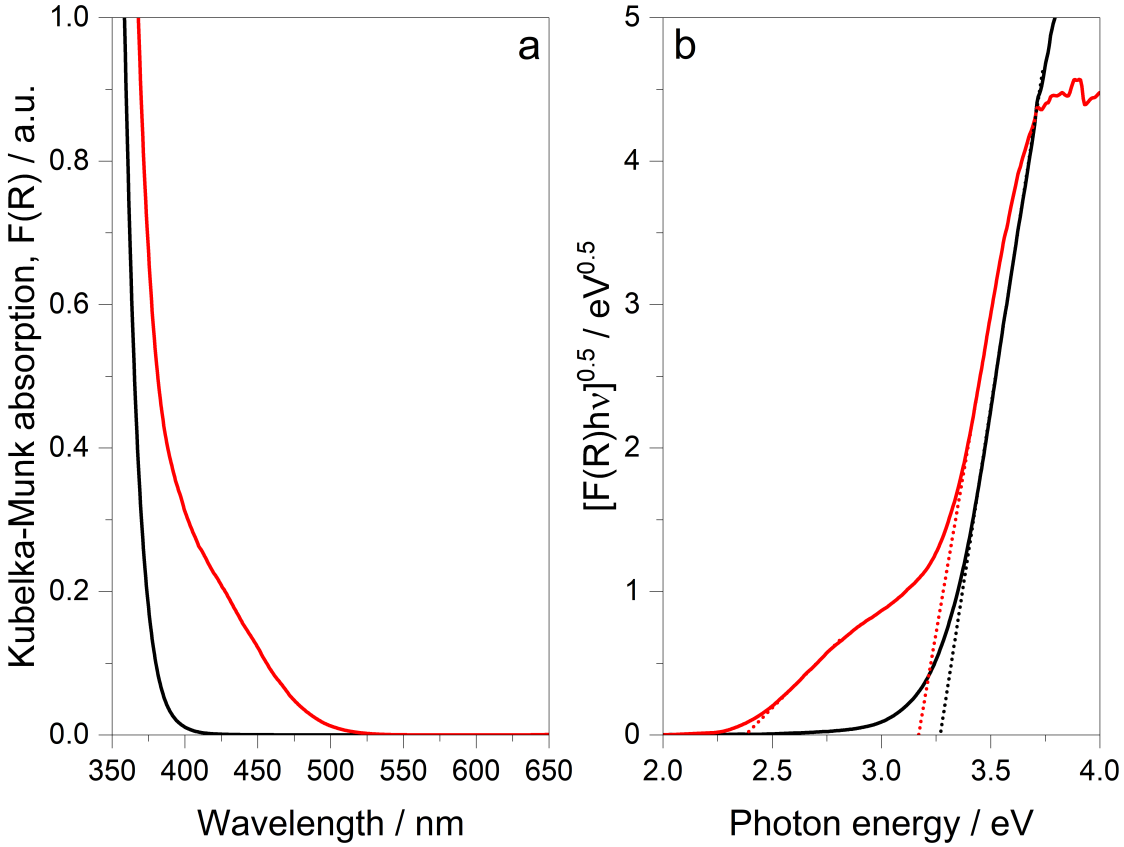

Figure 5: (a) UV-vis optical absorption spectra for the $Ti_{0.909}W_{0.091}O_2N_x$ sample (red) and undoped anatase TiO_2 (black) as a reference. (b) Tauc plot used to derive the optical intrinsic and extrinsic band gap values for the $Ti_{0.909}W_{0.091}O_2N_x$ sample (red). The Tauc plot of undoped anatase TiO_2 (black) is reported as a reference.

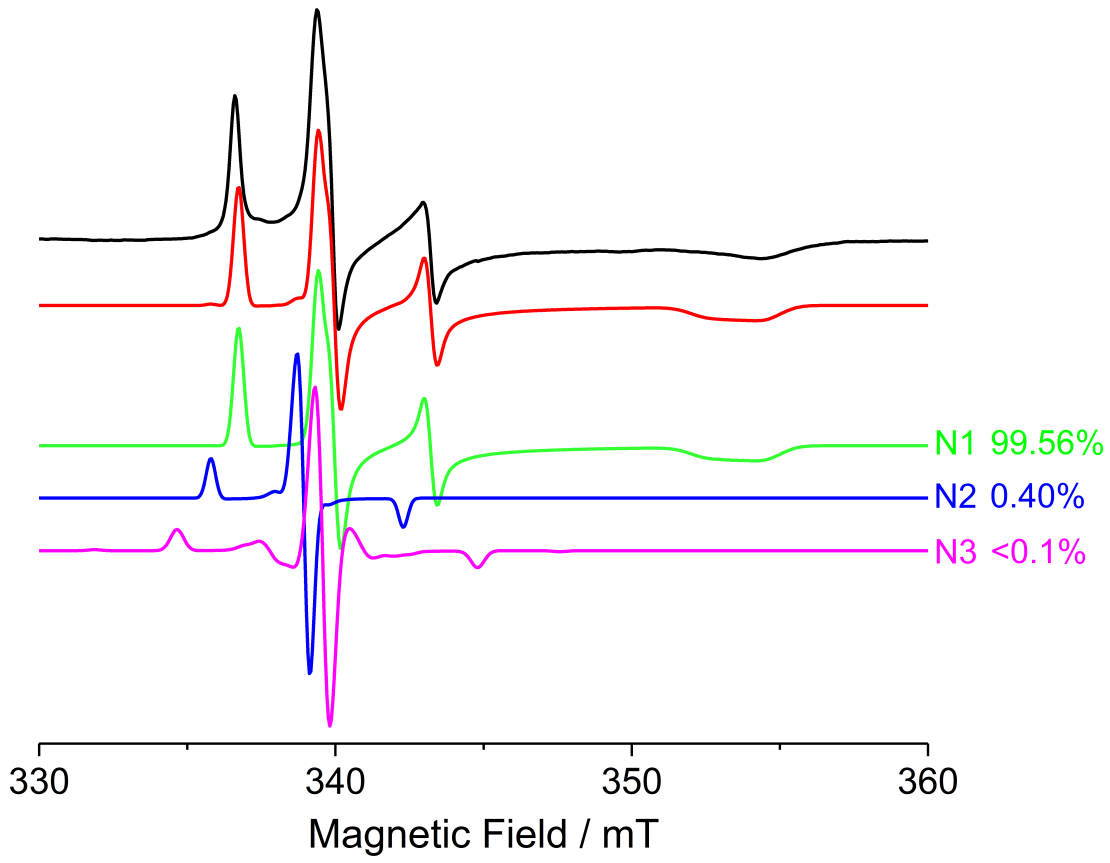

Figure 6: Experimental (black) and simulated (red) X-band CW EPR spectra of the $Ti_{0.909}W_{0.091}O_2N_x$ nanoparticles measured at 50 K around the free spin region. The simulated spectrum is deconvoluted into its three components N1 (green), N2 (blue) and N3 (magenta). The relative spectral contributions are also reported in the Figure. The experimental spectrum was recorded at 100 kHz field modulation frequency; 0.2 mT field modulation amplitude; 2 µW microwave power and 72 dB receiver gain. g and A values are listed in Table 2.

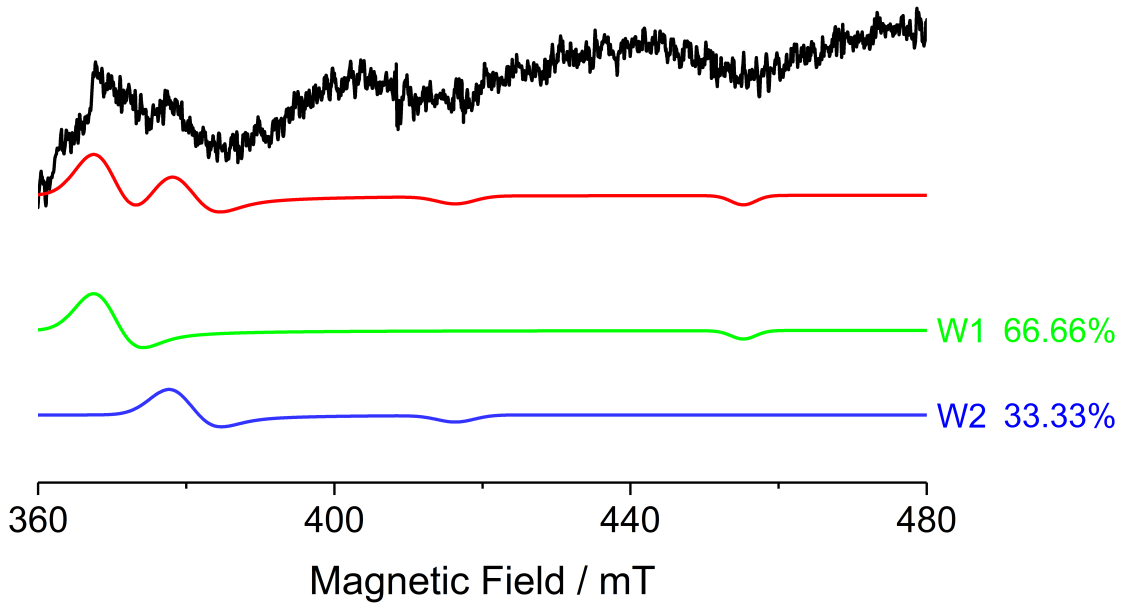

Figure 7: Experimental (black) and simulated (red) X-band CW EPR spectra of the $Ti_{0.909}W_{0.091}O_2N_x$ nanoparticles measured at 50 K at high fields. The simulated spectrum is deconvoluted into its two components W1 (green), W2 (blue). The relative spectral contributions are also reported in the Figure. The experimental spectrum was recorded at 100 kHz field modulation frequency; 0.2 mT field modulation amplitude; 2 µW microwave power and 72 dB receiver gain. g and A values are listed in Table 3.

Table 2: Spin Hamiltonian parameters of the NO centres.

	Species	Temp. / K	g_1	g_2	g_3	$\lvert A_1^{^{14}\mathrm{N}}\rvert$ / MHz	$\lvert A_2^{^{14}\mathrm{N}}\rvert$ / MHz	$\lvert A_3^{^{14}\mathrm{N}}\rvert$ / MHz	$\lvert A_1^{^{183}\mathrm{W}}\rvert$ / MHz	$\lvert A_2^{^{183}\mathrm{W}}\rvert$ / MHz	$\lvert A_3^{^{183}\mathrm{W}}\rvert$ / MHz	Rel. Cont. %	Ref.
N1	ads NO	50	2.001[a]	1.998[a]	1.921[a]	<2.8[b]	89.7[c]	26.9[c]				99.56 (95.24)[d]	Present work
		77	2.003	1.998	1.927	<2.8	89.7	26.9					43
		77	2.001	1.998	1.927	<2.8	90.2	26.9					40
N2	NO^{2-}	50	2.005[a]	2.004[a]	2.003[a]	6.5[c]	15.7[c]	89.7[c]				0.40 (3.81)[d]	Present work
		77	2.005	2.004	2.003	6.5	15.7	89.7					43
		77	2.005	2.004	2.003	6.5	12.3	90.2					40
N3	W-NO^{2-}	50	2.001[a]	2.000[a]	1.999[a]	42.0[c]	22.4[c]	140.1[c]	44.8[c]	<2.8[b]	154.1[c]	<0.1 (0.95)[d]	Present work
		77	2.002	2.001	2.000	22.4	22.4	140.1	44.8	<2.8	61.7		43

[a] $\pm$ 0.001; [b] not accurately measured; [c] $\pm$ 2.8MHz; [d] values in brackets refer to the relative contribution under light irradiation.

Table 3: Spin Hamiltonian parameters of the W^{5+} centres.

	Species	Temp. / K	$g_\perp$	$g_\parallel$	$\lvert A_\perp^{^{183}\mathrm{W}}\rvert$ / MHz	$\lvert A_\parallel^{^{183}\mathrm{W}}\rvert$ / MHz	Rel. Cont. %	Ref.
W1	W^{5+} in W_xO_y on $Ti_{0.909}W_{0.091}O_2N_x$	50	1.85[e]	1.50[e]	not observed	not observed	66.66	Present work
	W^{5+} in W_xO_y on ZrO_2	77	1.85	1.51	not observed	not observed		[48,49]
W2	W^{5+} in bronze struct. on $Ti_{0.909}W_{0.091}O_2N_x$	50	1.80[e]	1.64[e]	not observed	not observed	33.33	Present work
	W^{5+} in bronze struct. on ZrO_2	77	1.82	1.58	not observed	not observed		[48,49]
	W^{5+} in $(NH_4)_{0.27}WO_3$	77	1.80	1.56	not observed	not observed		[48,49]

[e] ± 0.01.

2.2 Photochemical response

The spectral contributions of the N2 and N3 centres to the overall EPR spectrum of the as synthesised $Ti_{0.909}W_{0.091}O_2N_x$ nanoparticles (Figure 6) is very low since a great majority of the $N_iO^{\bullet}$ species are diamagnetic (2 paired electrons in the highest occupied π^* antibonding orbital) before irradiation.[37,42] They can be seen as a N_iO^- species, i.e. intraband gap NO^{3-} states, and were proved to be energetically favourable over $N_iO^{\bullet}$ in the absence of irradiation.[37,42] The dark spectrum is therefore dominated by the signal of the encapsulated adsorbed molecular NO (N1 center). Upon irradiation with light having energy - at least - equal to the extrinsic band gap of 2.38 ± 0.02 eV, electron transitions CB$\leftarrow NO^{3-}$ occur, generating a much larger amount of paramagnetic NO^{2-} states, as indicated by the increase in signal amplitude associated with the N2 and N3 centres in Figure 8b (main features indicated by arrows). These spectral changes match what has been previously reported for similar N-doped TiO_2 samples.[37,40,42,43,46] The EPR spectrum recorded under light irradiation is also reported in the SI at higher resolution with overall simulation; deconvolution of the N1, N2 and N3 signals and their relative spectral contributions. Our findings here reported also show that the N1 centre signal amplitude decreases upon light irradiation. This evidence is not completely understood yet and this phenomenon is currently under further investigation in our laboratories. A possible explanation could be that if the encapsulated molecular NO is adsorbed on a subsurface oxygen vacancy (i.e. a cationic crystal defect and therefore allowing molecular NO to show the g-values reported in (Table 2)) and the oxygen vacancy acts as an electron trapping centre for conduction band electrons formed upon light irradiation, reduction of NO could occur:[40]

$$NO + V_O + 2e^- \rightarrow NO^{2-} \quad (1)$$

resulting in a NO^{2-} radical anion occupying the volume of an oxygen vacancy. Its electronic configuration would be that of a 13 electrons $^2\Pi_{3/2}$ radical anion with the unpaired

electron in a π^* antibonding orbital,[40] i.e. a π system completely indistinguishable from the NO^{2-} discussed previously (N2 and N3 centres) and formed upon electron transitions from an NO^{3-}. Around the free spin region, there was no evidence on the formation of a detectable amount of Ti^{3+} upon light irradiation.

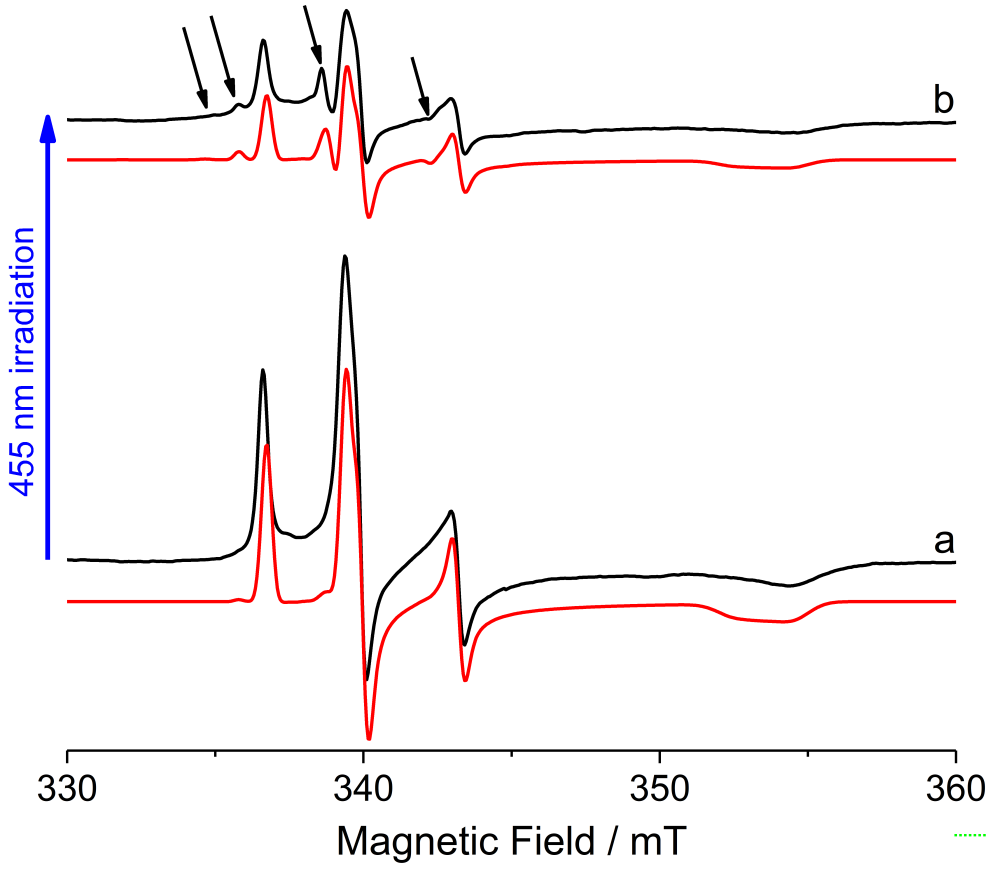

Figure 8: Experimental (black) and simulated (red) X-band CW EPR spectra of the $Ti_{0.909}W_{0.091}O_2N_x$ nanoparticles measured at 50 K around the free spin region (a) before and (b) during irradiation with a 455 nm LED light source. The experimental spectra were recorded at 100 kHz field modulation frequency; 0.2 mT field modulation amplitude; 2 µW microwave power and 72 dB receiver gain.

.

.

At higher fields, the EPR signal of the surface W^{5+} centres was found to increase in intensity following visible light irradiation at 455 nm (Figure 9). This could be explained by electron transition from the mid-gap N-doping donor level to the conduction band of the semiconductor (as seen above) followed by electron trapping in the form of W^{5+}. Elec-

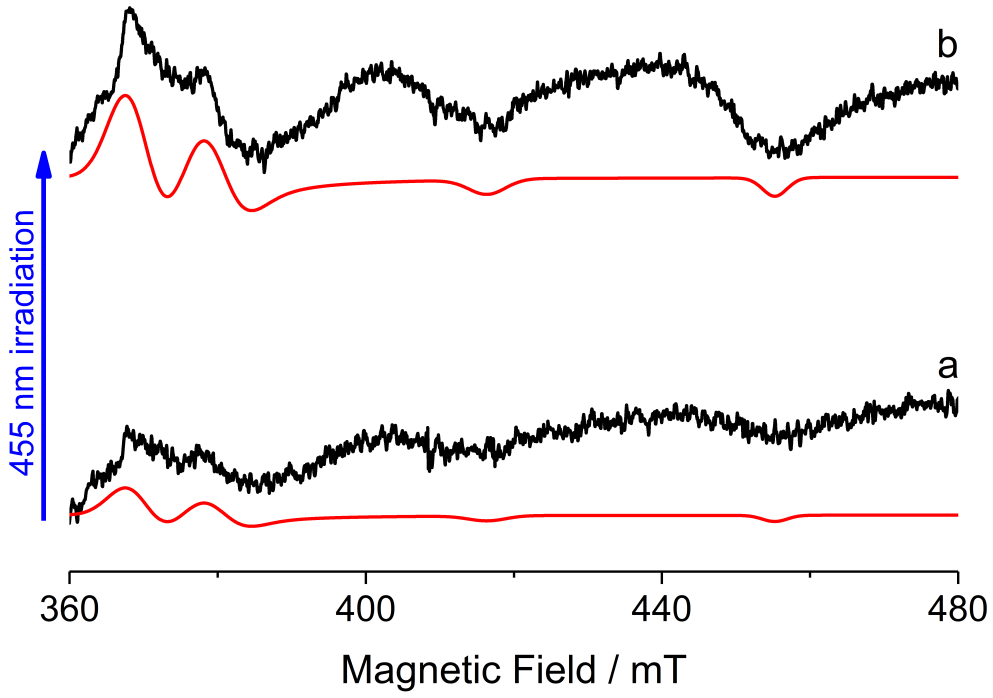

Figure 9: Experimental (black) and simulated (red) X-band CW EPR spectra of the $Ti_{0.909}W_{0.091}O_2N_x$ nanoparticles measured at 50 K at high fields (a) before and (b) during irradiation with a 455 nm LED light source. The experimental spectra were recorded at 100 kHz field modulation frequency; 0.2 mT field modulation amplitude; 2 µW microwave power and 72 dB receiver gain.

tron transitions from the valence band of the semiconductor nanoparticles to a W^{5+} level cannot be excluded at this stage. Contrary to the case of pristine TiO_2 (in particular the anatase and brookite polymorphs) where shallow trapped electrons in the form of surface Ti^{3+} readily reduce molecular oxygen to superoxide anions, $O_2^{\bullet-}$, trapped electrons in these W containing nanoparticles were found to be highly stable at room temperature even in the presence of molecular oxygen, as suggested by photo-charging events (Figure 10a and b) followed by measuring the absorbance at 800 nm exhibited by the nanoparticles in the presence of molecular oxygen and under light irradiation. W bronzes/W^{5+} polarons show broad absorption from the red into the near-IR, and that this is why absorption increases at 800 nm when W^{5+} centres are formed upon photo-irradiation of the sample with broad band light (300 to 2000 nm). Photo-generated electrons in undoped TiO_2 also absorb at 800 nm, and more strongly so in the presence of an alcohol hole scavenger.[51] Nevertheless, taken into consideration the difference in molar extinction coefficients at 800 nm, ϵ_λ^{800}, between trapped electrons in TiO_2, estimated in the range 500 to 600 $L\,mol^{-1}\,cm^{-1}$,[52,53] and trapped electrons in WO_3 ($W^{5+}\rightarrow W^{6+}$ intervalence charge-transfer (IVCT), also applicable to our nanoparticles), of 7300 $L\,mol^{-1}\,cm^{-1}$,[54] the 50 times larger absorbance at 800 nm for $Ti_{0.909}W_{0.091}O_2N_x$ nanoparticles compared to undoped TiO_2, corresponds to 3.4 to 4.1 times larger stored electrons concentration. The direct involvement of W-oxo species in the electron storage was proved by diminishing the amount of W in the nanoparticles, which resulted in a lower stored electron concentration (Figure 10a and b). These observations are in agreement with results obtained by other researchers on TiO_2/WO_3 mixed oxide systems.[24–29] The presence of W in oxidation states lower than 6 would make the oxide quasi-metallic or metallic[55,56] which could be an independent confirmation of bronze-like chemistry. Indeed, EPR spectra at low magnetic fields (Figure 11) exhibited a broad, asymmetric signal, typical of a dysonian line[57] which is symptomatic of conduction electrons diffusing through a skin depth layer.[57]

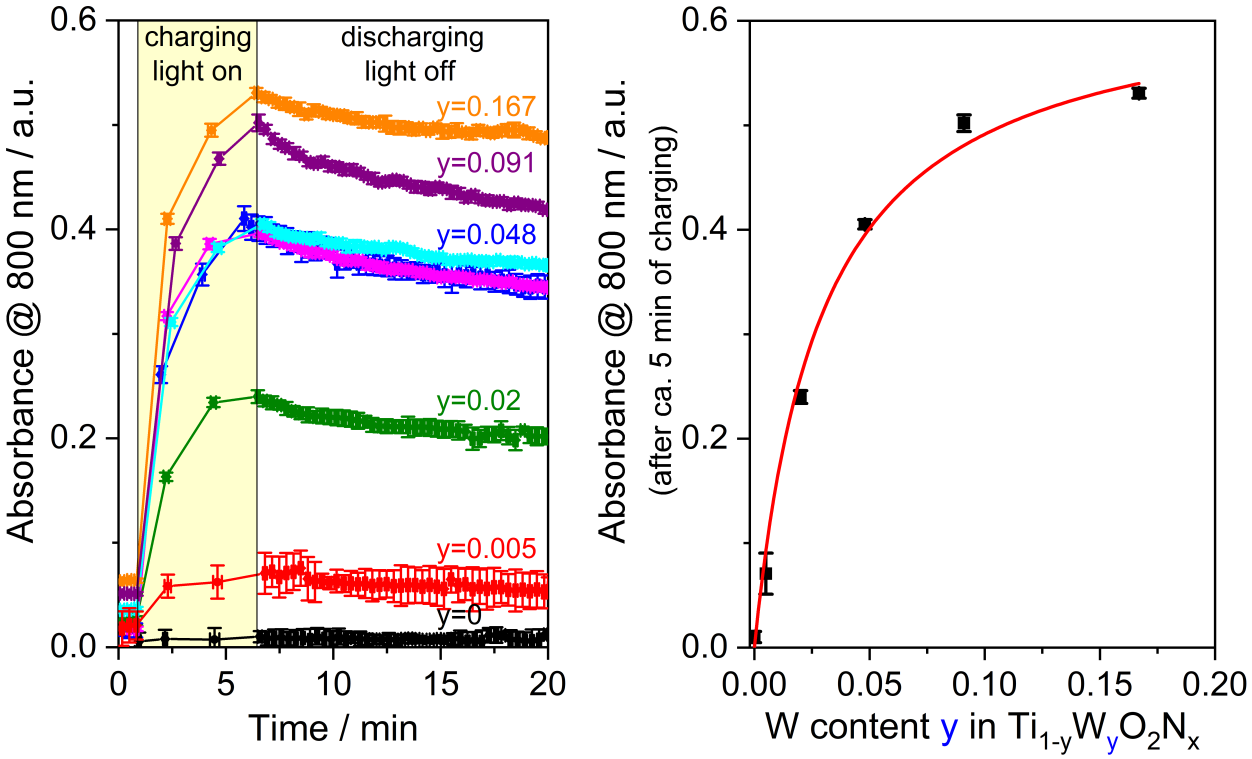

Figure 10: (a) Electron storage ability of the $Ti_{1-y}W_yO_2N_x$ powder nanoparticles in air measured as absorbance profiles at 800 nm upon charging with a broad band (ca. 300 to 2000 nm) light source, in the presence of a hole scavenger (isopropanol), and during discharging (i.e. after turning the light off). The dependency of the amount of electrons stored on the W content in the nanoparticles is highlighted in (b), showing an increase of the absorbances after 5 minutes of irradiation as a function of the W loading.

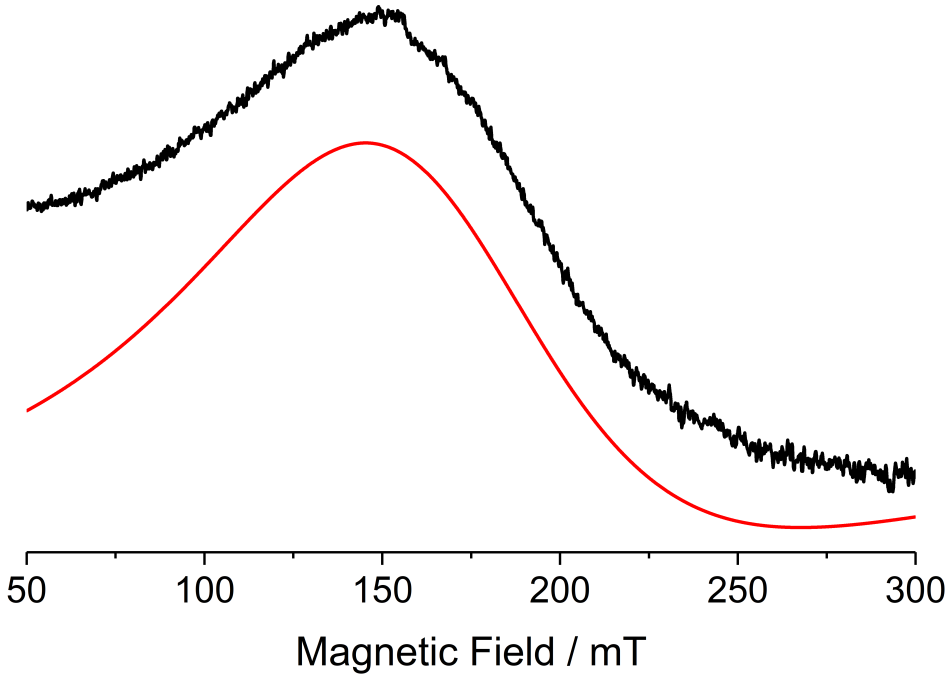

Figure 11: Representative X-band CW EPR spectra at 50 K of $Ti_{0.909}W_{0.091}O_2N_x$ at low field showing the broad, asymmetric dysonian line-shaped signal associated with the presence of conduction electrons diffusing through a layer of particles dependent on the skin depth of the microwave radiation. The spectrum was simulated using the Dyson function and analysis reported in the SI, which led to the following optimised parameters: asymmetry parameter $\alpha = 2.7$, position of the resonance line, H_0 =165 mT and width of the resonance line, ΔH =190 to 200 mT. The experimental spectrum was recorded at 100 kHz field modulation frequency; 0.2 mT field modulation amplitude; 2 µW microwave power and 72 dB receiver gain.

2.3 Electrochemical Oxygen Reduction Reaction (ORR)

Undoped TiO_2 is known for showing almost negligible oxygen reduction current at positive potentials with measurable current only at potentials vs. RHE lower than +0.3 V;[58] this was here proved again (black current profile in Figure 12). The accepted view is that undoped TiO_2 mainly promotes a single electron transfer (SET) to molecular oxygen generating superoxide radical, $O_2^{\bullet-}$. On the contrary, electrochemical characterisation of the $Ti_{1-y}W_yO_2N_x$ powder nanoparticles (red current profile in Figure 12 exemplifies the case of ca. 5 at.% W loading corresponding to the threshold above which the absorbance at 800 nm in Figure 10b and the nitrate selectivity in Figure 14b approach limiting and maximum values), showed current at potentials as high as +0.6 V vs. RHE. This indicates *at least* a two electron reduction process (the standard redox potential for two electron reduction of oxygen to peroxide is +0.695 V vs. RHE). However, a two electron transfer normally proceeds with much slower kinetics compared to SET. This could explain the very slow discharging profile evident in Figure 10, which facilitates the storage of electrons for long periods of time (more than 12 hours were needed to completely discharge the material in air at ambient conditions). Neglecting the case of W^{3+} (EPR spectra were inconclusive as to the presence or absence of such reduced species), two electron transfer can mechanistically occur from either a W^{4+} centre or two neighbouring W^{5+} centres simultaneously transferring one electron each, in perfect agreement with the EPR data described above. At the present stage, we cannot completely exclude a potential role of the N centres too, given that N-doped TiO_2 had been previously reported in the literature as an oxide capable of two-electron transfer in the ORR;[59,60] although, the N doping was substitutional rather than interstitial like in our case. Further investigations are currently being conducted to decouple the actual contributions of the two dopants using electrochemical and spectroscopic methods combined with theoretical calculations. Nevertheless, and as far as the purpose of the present work is concerned, it is clear that $Ti_{1-y}W_yO_2N_x$ powder nanoparticles provide oxygen reduction routes that are not accessible by undoped TiO_2.

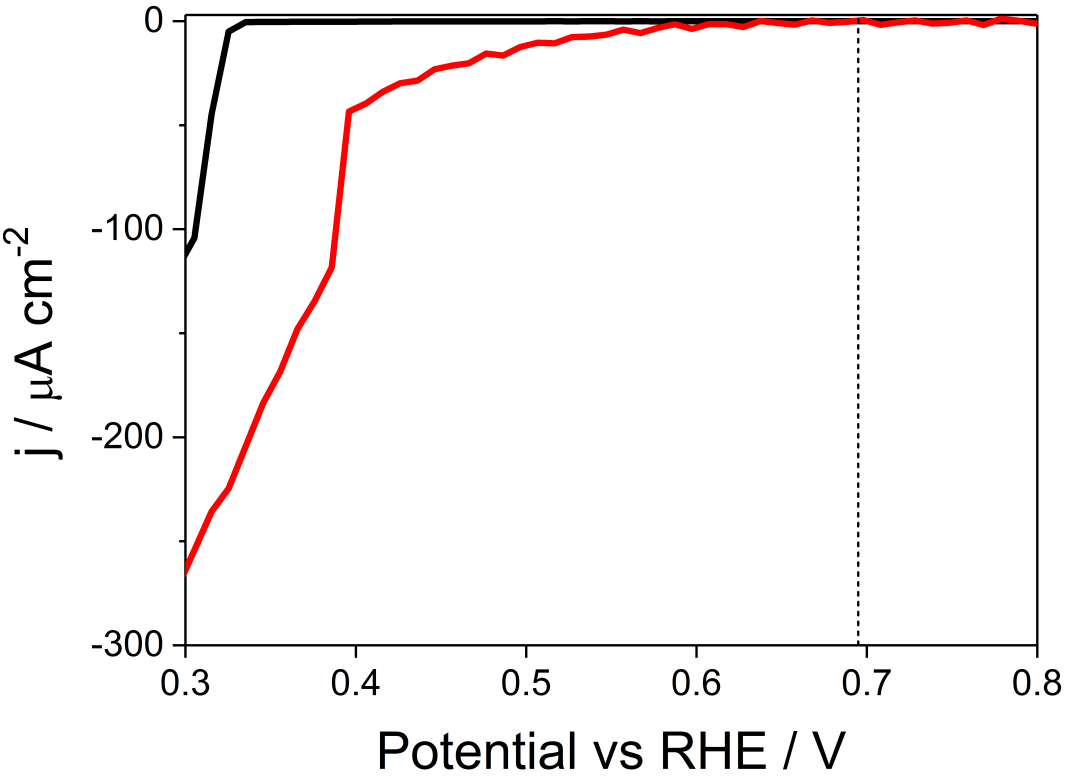

Figure 12: Oxygen reduction currents versus applied potential for undoped anatase TiO_2 nanoparticles (black trace) and $Ti_{0.952}W_{0.048}O_2N_x$ (red trace). For $Ti_{0.952}W_{0.048}O_2N_x$, the potential at which ORR starts (ca. 0.6 V vs RHE) and the Tafel slope of the current profile are indicative of a two electron reduction process.

2.4 Photocatalytic NOx abatement (DeNOx)

When $Ti_{1-y}W_yO_2N_x$ nanomaterials were employed as photocatalysts for the oxidation of nitric oxide, NO, to nitrates, NO_3^-, Figure 13, the undesired formation of the toxic NO_2 by-product dropped by a factor of up to 106, Figure 14a, when compared to anatase TiO_2. As a result, the nitrate selectivity increased from ca. 29 % for pristine anatase TiO_2 to ca. 90 % for $Ti_{0.909}W_{0.091}O_2N_x$, Figure 14b. The remarkable increase in selectivity is accompanied by a decrease in photonic efficiency of NOx removal by a factor of about 3, Figure 14c. Amongst the possible reasons for this drop in photonic efficiency are: i. loss in potential energy of photo-generated electrons when they relax from the conduction band of TiO_2 into localised W^{5+} states; ii. positive holes localised in the N intraband gap states not possessing a redox potential high enough to generate $^{\bullet}OH$ from water.[32,43] However, the overall DeNOx index representing the relative change in nitrogen oxide-associated air toxicity combining photonic efficiency, selectivity and relative toxicity in one single parameter,[7] showed improvement of air quality (i.e. positive DeNOx index) for samples with W content higher than 5 at.%. This is in contrast to the case of undoped TiO_2, where the very high activity but inadequate selectivity (<50 %) could potentially increase rather than decrease the air toxicity, due to predominant formation of undesired and toxic NO_2[32,61] (see also[7] for comparison of W and N containing TiO_2 with benchmark TiO_2 photocatalyst P25 and other commonly used commercially available TiO_2 photocatalysts). An ideal photocatalyst for DeNOx processes would have the valence band photo-generated holes driving the one electron stepwise oxidation of NO to NO_3^-[62,63] and the conduction band electrons scavenged by molecular oxygen. However, nitrate ions that are formed are not just a non-reactive end-product but lead to nitrate poisoning of the catalyst, resulting in lower activity but more significantly, in greatly reduced selectivity as nitrates can scavenge conduction band electrons resulting in a back-reduction of NO_3^- to NO_2; i.e. a SET process that on undoped TiO_2 is in competition with SET reduction of molecular oxygen to superoxide radical. Selectivity can also be compromised by NO_3^- scavenging a valence band photo-generated hole generating a NO_3 species that subse-

quently reacts with NO forming $2NO_2$ as shown by Ohko et al.[64] Whilst our rational design was not intended to act upon this latter process, we focused on the former back-reaction formation of NO_2 from NO_3^-. Specifically, we observed that enabling electron transfer processes that are kinetically inaccessible with undoped TiO_2, like a two electron reduction of molecular oxygen at potentials vs. RHE as high as + 0.5-0.6 V, through the co-catalysing oxygen reduction abilities of W and N in $Ti_{0.909}W_{0.091}O_2N_x$ nanoparticles, seems to have a beneficial effect on the selectivity given that the effective difference in reduction potentials of molecular oxygen and nitrate on the catalyst is significantly reduced and the relative reduction rates therefore greatly shifted towards the desired photo-generated electrons scavenging by molecular oxygen. This rationale was also confirmed by one of our recent studies involving simulations of NO_3^- and O_2 reduction kinetics on TiO_2.[61] Interestingly, when we evaluated catalysts which only had tungsten and no nitrogen, the nitrate selectivity was similar as for the case of the codoped catalysts,[7] which was not true for catalysts containing solely N and no W, which on the other hand exhibited selectivity similar to undoped TiO_2.[7] Accordingly, if the recent results by Yuan et al. and Seifitokaldani[59,60] about substitutional N-doped TiO_2 capable to catalyse multi-electron transfer to molecular oxygen are proven correct, it will stand to reason that either interstitial N doping cannot promote multiple electron transfer and/or new fundamental aspects of the co-catalytic mechanisms of W and N in TiO_2 have yet to be uncovered. Further investigations (including a series of other transition metal co-catalysts) are currently being performed in order to try to answer these still outstanding questions.

.

.

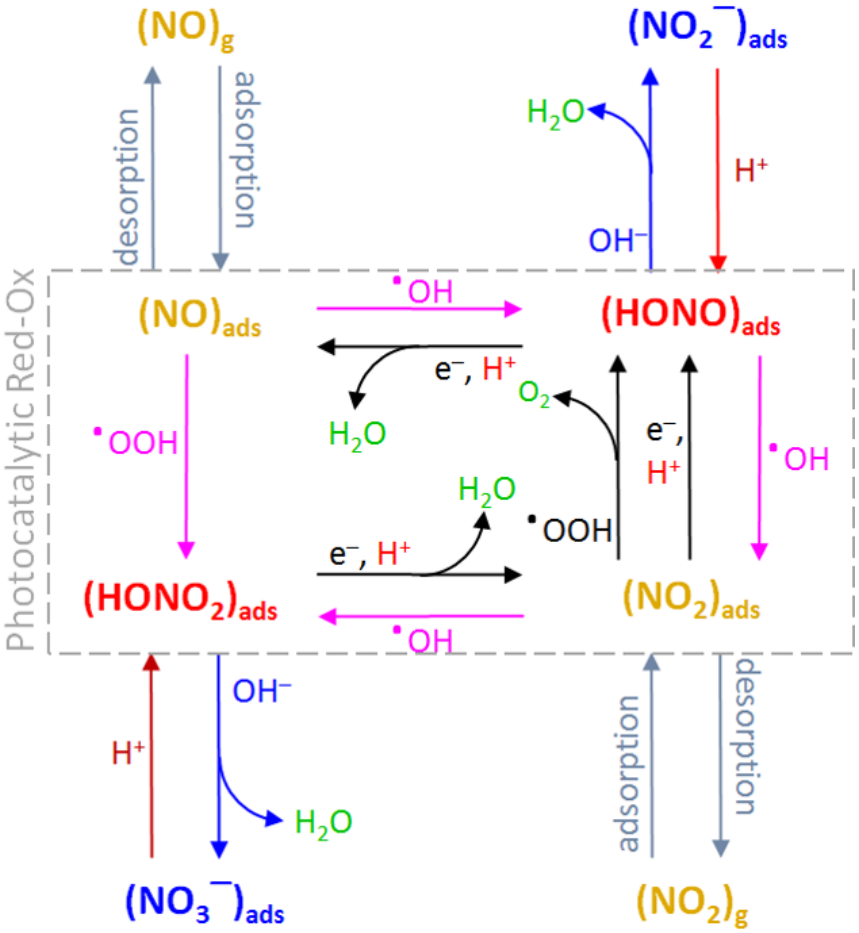

Figure 13: NO (and NO_2) photocatalytic oxidation/reduction pathways. The subscripts g and ads indicate species in the gas phase and adsorbed on the catalyst surface respectively.

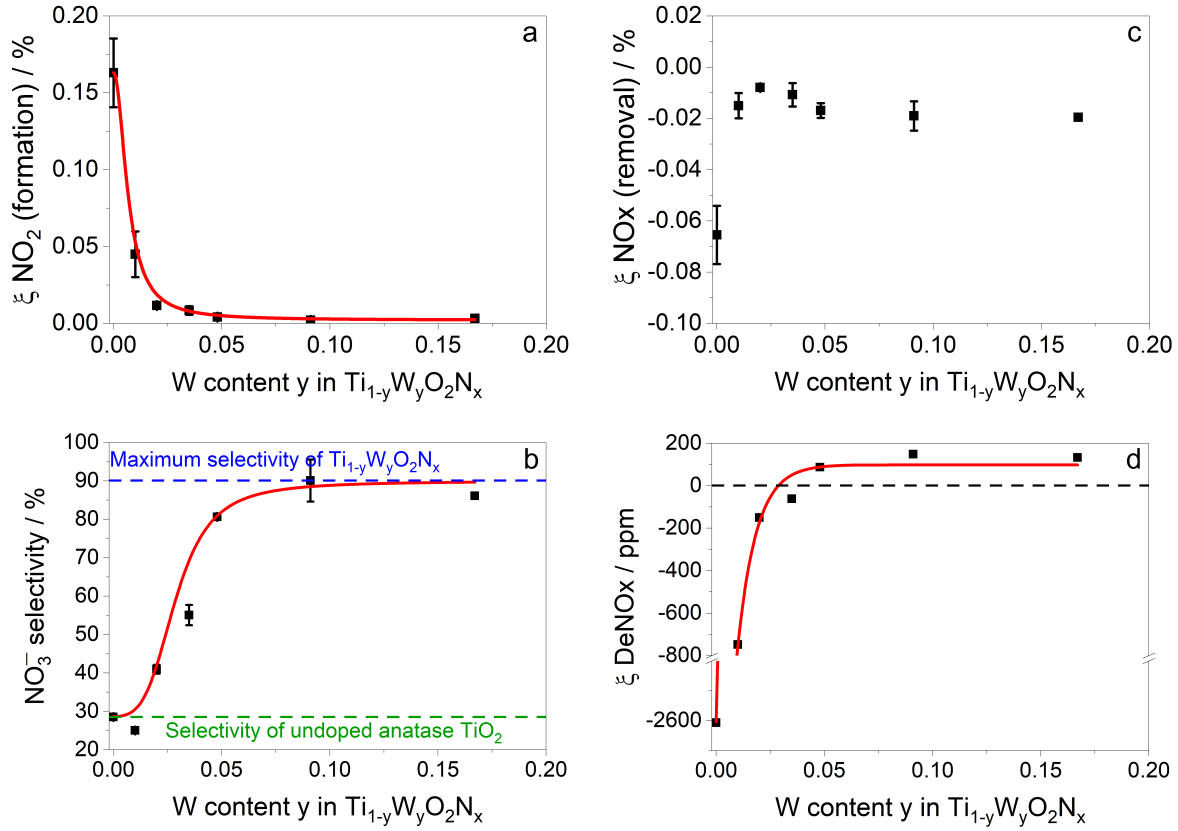

Figure 14: (a) Photonic efficiency of NO_2 formation *vs* W content y in $Ti_{1-y}W_yO_2N_x$ nanomaterials. (b) Selectivity of NO photocatalytic oxidation with respect to nitrate (i.e. desired product) formation *vs* W content y in $Ti_{1-y}W_yO_2N_x$. (c) Photonic efficiency of overall NOx removal *vs* W content y in $Ti_{1-y}W_yO_2N_x$. (d) DeNOx index *vs* W content y in $Ti_{1-y}W_yO_2N_x$; positive values indicate improvement of air quality while negative values indicate deterioration of air quality.

3 Conclusions

In conclusion, in $Ti_{0.909}W_{0.091}O_2N_x$ semiconductor nanoparticles an extrinsic optical band gap of 2.38 ± 0.02 eV, due to the presence of intra-band gap NO states, was observed together with an intrinsic optical band gap of 3.17 ± 0.01 eV typical of TiO_2. Upon light irradiation, NO^{2-} states are generated by electronic transitions from the intra-band gap NO^{3-} to the CB, with spin density associated with NO^{2-} states polarised by the presence of close range interactions with polarising W ions, potentially affecting the reactivity/electrochemistry of NO^{2-} states when compared to the case of solely N doped TiO_2. Photo-generated conduction band electrons were also observed to be trapped in W^{5+} states, which were found to be more stable compared to Ti^{3+} states in undoped TiO_2, and can therefore be linked to the higher electron storage ability at ambient conditions, often exhibited by TiO_2/WO_3 mixed oxides over undoped TiO_2. Electrons stored in these semiconductor nanoparticles were shown here to be discharged to molecular oxygen via a two electron transfer event at redox potentials much higher than the typical superoxide formation via SET reaction, even in the absence of light. The fact that the two electron reduction of molecular oxygen is kinetically accessible for $Ti_{0.909}W_{0.091}O_2N_x$ (it is not in the case of undoped TiO_2) shifts the competition for scavenging electrons towards the desired oxygen reduction rather than nitrate reduction to NO_2, which could help to explain why $Ti_{0.909}W_{0.091}O_2N_x$ exhibits such a higher nitrate selectivity when compared to undoped TiO_2.

Together with providing a clear electronic-crystallographic-structural relationship for $Ti_{1-y}W_yO_2N_x$ semiconductor nanoparticles, explaining the mutual electronic and magnetic influence of the photo-induced, stable N- and W-based paramagnetic centres, this research provides some new fundamental insight and understanding of the association between improved oxygen reduction and improved nitrate selectivity in the photocatalytic DeNOx process of removal of harmful nitrogen oxides. Further effort should therefore be spent to fully comprehend the extent of benefits coming from multiple oxygen reduction pathways and how to finely tune them, with catalyst modifications that improve selectivity without

compromising overall activity.

4 Materials and Methods

Synthesis

For a typical preparation of the $Ti_{1-y}W_yO_2N_x$ nanoarchitectures, 10 mL of titanium isopropoxide (≥97 %, Sigma-Aldrich), were dissolved in 10 mL of anhydrous ethanol. After thoroughly mixing the solution, 5 mL of deionised water (18 MΩ cm) were slowly added to the solution. The resulting white precipitate formed a well dispersed, white sol upon further stirring. Ammonium tungstate (BDH Chemicals), in the necessary amount to achieve a 10 at.% substitution for Ti (or lower loadings as for other samples reported in this work), was then dissolved in 10 mL of warm deionised water and subsequently added to the solution. After thorough stirring for at least 4 h, the solution was filtered. The solid was washed with deionised water and then dried at 373 K for at least 4 h. The dry powders were ground in an agate mortar and then transferred into a crucible for calcination. The samples were calcined at 873 K for 4 h and ground again after calcination.

Neutron Diffraction

Neutron powder diffraction data were collected on the General Materials Diffractometer (GEM) at the ISIS pulsed spallation neutron source, Rutherford Appleton Laboratory, UK. Neutron diffraction patterns were measured at 303 K from a 5 g sample loaded in an 8 mm diameter thin-walled vanadium sample can for 225 µA h proton beam current to the ISIS target (corresponding to ca. 1.5 h collection time). The crystal structure was refined by the Rietveld method from data collected in the low angle, 90° and backscattering detector banks, average $2\theta = 63°$, 92° and 154° respectively, and covering a d-spacing range from 0.42 to 4 Å. The GSAS program with the EXPGUI interface[65] was used for the refinement.

X-Ray Photoelectron Spectroscopy (XPS)

A Kratos Axis Ultra DLD system was used to collect XPS spectra using monochromatic Al Kα X-ray source operating at 140 W (10 mA x 14 kV). Data was collected with pass energies of 80 eV for survey spectra, and 40 eV for the high-resolution scans with step sizes of 1 eV and 0.1 eV respectively. The system was operated in the Hybrid mode, using a combination of magnetic immersion and electrostatic lenses and acquired over an area approximately 300 x 700 µm^2. A magnetically confined charge compensation system was used to minimize charging of the sample surface; all spectra were calibrated to the C(1s) line for adventitious carbon taken to be 284.8 eV. A base pressure of ca. 10^{-9} torr was maintained during collection of the spectra. Data was analysed using CasaXPS (v2.3.19rev1.2) after subtraction of a Shirley background and using modified Wagner sensitivity factors as supplied by the manufacturer.

Scanning Transmission Electron Microscopy (STEM)

Samples for examination by scanning transmission electron microscopy (STEM) were prepared by dispersing the dry catalyst powder onto a holey carbon film supported by a 300 mesh copper TEM grid. STEM high angle annular dark field (HAADF) images of the samples were obtained using an aberration corrected JEM ARM-200CF STEM operating at 200 kV.

UV-vis Diffuse Reflectance Spectroscopy

UV-vis diffuse reflectance spectra were collected on a StellarNet EPP2000 spectrophotometer with barium sulfate as a reference in the range of 350 to 650 nm. The resulting reflectance spectra were transformed into apparent absorption spectra by using the Kubelka-Munk function (Equation 2).

$$F(R_\infty) = \frac{(1 - R_\infty)^2}{2R_\infty} \quad (2)$$

The apparent absorption spectra were subsequently used to determine the optical band gap of the materials by constructing Tauc plots for indirect band gap semiconductors, by plotting $(F(R_\infty)h\nu)^{1/2}$ against $h\nu$. The indirect optical band gaps were obtained by extrapolating the linear part of these plots to the x-axis (i.e. photon energy).

Electron Paramagnetic Resonance Spectroscopy (EPR)

The X-band CW-EPR spectra were recorded on a Bruker Elexsys E500 spectrometer equipped with an Oxford Instruments liquid-helium cryostat and a Bruker ER4122 SHQE-W1 super high Q resonator, operating at 50 K. Before each measurement, the samples were evacuated for at least 12 hours at 393 K and under dynamic vacuum, ca. 10^{-4} bar. Spectra were recorded in darkness and after in situ irradiation (in the spectrometer cavity) with a Labino Nova Torch 455 nm LED light source (20 nm bandwidth centred around the main wavelength). Experimental spectra were simulated using the EasySpin package[66] operating within the Mathworks Matlab environment.

Electrochemical oxygen reduction reaction

Electrochemical oxygen reduction reaction (ORR) measurements required the fabrication of electrodes from the semiconducting material prior to the experiment. The electrodes were prepared by electrophoretic deposition of the semiconducting solid on conductive glass (fluorine-doped tin oxide, FTO). Square slides (25 x 25 mm^2) of FTO (Sigma-Aldrich, 7 $\Omega/\square$) were ultrasonically cleaned in acetone and water and then dried at ambient conditions. A coating ink was prepared by ultrasonically dispersing 100 mg of the sample in 100 mL of a 0.1 mmol L^{-1} ammonia solution. The FTO glass slides were coated by using electrophoretic deposition, in a cell where the FTO glass was used as anode and a platinum mesh as cathode. The deposition was performed at a potential of +15 V for 10 minutes. After deposition, the coated electrode was very carefully washed with deionised water and annealed at 673 K for 1 hour. The ORR measurements were performed in a 3-electrode cell with the coated FTO-Glass as a working electrode, a coiled platinum wire as a counter electrode, and a Ag/AgCl reference electrode (3 mol L^{-1} NaCl, +205 mV vs SHE). The electrodes were placed in the measurement cell making sure that in the case of the working electrode only the coated part of the FTO-Glass would be in contact with the 0.1 mol L^{-1} KOH electrolyte. O_2 was continuously bubbled in the electrolyte solution during the measurement.

Electron storage performance

For the electron storage experiment in air and ambient condition, 0.05 mL of isopropyl alcohol (hole scavenger) and 80 mg of catalyst were mixed and kept in air and darkness for 10 min to ensure adsorption of isopropyl alcohol on the surface of the photocatalyst. The wet powder was then placed on a plate and irradiated using a UV-A lamp (Osram Ultra-Vitalux) with a photon flux at the level of the powder sample equal to 5.268×10^{-5} mol s^{-1} m^{-2}. The change in the optical absorption of the photocatalytic powder was monitored using a Perkin Elmer Lambda 750 UV/Vis/NIR spectrophotometer in the diffuse reflectance mode.

DeNOx performance

Measurements of the photonic efficiency/selectivity of the oxidation of nitric oxide were carried out in a glass flow-through reactor[63] with the powder sample placed on a glass grit inside the reactor (allowing the pollutant gas to pass through) and irradiated from the top through an optical window. An Ultra-Vitalux 300 W (Osram, Germany) light source was employed as the light source for irradiation with a photon flux at the position of the powder sample equal to 5.268×10^{-5} mol s^{-1} m^{-2} determined using ferrioxalate actinometry.[67–69] 0.3 g of the sample was uniformly distributed on the circular glass grit with an area of 8.042×10^{-4} m^2 inside the reactor. The pollutant gas, i.e. synthetic air containing 8 ppm of NO (volumetric flow rate 8.33×10^{-7} m^3 s^{-1}) was then flowed through the reactor. The temperature was controlled using a water jacked around the reactor connected to thermostat and was monitored and kept constant at 300 K. Prior to entering the reactor, the air

was humidified and kept at a constant 42 % relative humidity. The concentrations of NO, NO_2 and total NO_x in the outlet gas flow were monitored using a Thermo Scientific Model 42i-HL High Level NO-NO_2-NOX Analyzer (Air Monitors Ltd., United Kingdom). Measurements were conducted in the dark until equilibrium concentration was reached and subsequently under irradiation until steady state concentrations were observed (normally after ca. 20 h). The photonic efficiency ξ was calculated according to eq. 3, where c_d is the concentration under dark conditions, c_i the concentration under illumination, $\dot{V}$ the volumetric flow rate, p the pressure, A the irradiated area, R the gas constant, T the absolute temperature and Φ the photon flux impinging the photocatalyst surface as determined by actinometry. Photonic efficiencies for NO, NO_2 and total NO_x were determined separately.

$$\xi = \frac{(c_d - c_i) \cdot \dot{V} \cdot p}{\Phi \cdot A \cdot R \cdot T} \tag{3}$$

The nitrate selectivity (i.e. the amount of NO effectively converted to nitrate rather than nitrogen dioxide) was derived according to eq. 4.

$$S = \frac{\xi_{NOx}}{\xi_{NO}} \tag{4}$$

Finally, the DeNOx index[7] was calculated according to eq. 5, where ξ_{NO} and ξ_{NO2} represent the photonic efficiencies of NO removal and NO_2 formation, respectively, and S the selectivity towards nitrate formation according to eq. 4:

$$\xi_{DeNOx} = \xi_{NO} - 3 \cdot \xi_{NO2} \tag{5}$$

5 Supporting Information

The Supporting Information is available free of charge on the ACS Publications website. X-band CW EPR spectra under irradiation. Dyson line simulation and analysis.

References

(1) Fujishima, A.; Honda, K. Electrochemical Photolysis of Water at a Semiconductor Electrode. *Nature* **1972**, *238*, 37–38.

(2) Maldonado, M. I.; Blanco, J.; Gernjak, W.; Malato, S.; Ferna, P. Decontamination and Disinfection of Water by Solar Photocatalysis : Recent Overview and Trends. *Catal. Today* **2009**, *147*, 1–59.

(3) Fujishima, A.; Rao, T. N.; Tryk, D. A. Titanium Dioxide Photocatalysis. *J. Photochem. Photobiol. C* **2000**, *1*, 1–21.

(4) Mills, A.; Le Hunte, S. An overview of Semiconductor Photocatalysis. *J. Photochem. Photobiol. A* **1997**, *108*, 1–35.

(5) Hoffmann, M. R.; Martin, S. T.; Choi, W.; Bahnemann, D. W. Environmental Applications of Semiconductor Photocatalysis. *Chem. Rev.* **1995**, *95*, 69–96.

(6) Ballari, M. M.; Brouwers, H. J. H. Full scale Demonstration of Air-Purifying Pavement. *J. Hazard. Mater.* **2013**, *254-255*, 406–414.

(7) Bloh, J. Z.; Folli, A.; Macphee, D. E. Photocatalytic NOx Abatement: Why the Selectivity Matters. *RSC Adv.* **2014**, *4*, 45726–45734.

(8) Folli, A.; Strøm, M.; Pilegaard Madsen, T.; Henriksen, T.; Lang, J.; Emenius, J.; Klevebrant, T.; Nilsson, Å. Field Study of Air Purifying Paving Elements Containing TiO2. *Atmos. Environ.* **2015**, *107*, 44–51.

(9) Auvinen, J.; Wirtanen, L. The Influence of Photocatalytic Interior Paints on Indoor Air Quality. *Atmos. Environ.* **2008**, *42*, 4101–4112.

(10) Dillert, R.; Engel, A.; Große, J.; Lindner, P.; Bahnemann, D. W. Light Intensity Dependence of the Kinetics of the Photocatalytic Oxidation of Nitrogen(II) Oxide at the Surface of TiO2. *Phys. Chem. Chem. Phys.* **2013**, *15*, 20876–86.

(11) Folli, A.; Pade, C.; Hansen, T. B.; De Marco, T.; Macphee, D. E. TiO2 Photocatalysis in Cementitious Systems: Insights into Self-Cleaning and Depollution Chemistry. *Cem. Conc. Res.* **2012**, *42*, 539–548.

(12) Zhao, J.; Yang, X. Photocatalytic Oxidation for Indoor Air Purification: a Literature Review. *Build. Environ.* **2003**, *38*, 645–654.

(13) Lasek, J.; Yu, Y. H.; Wu, J. C. S. Removal of NOx by Photocatalytic Processes. *J. Photochem. Photobiol. C* **2013**, *14*, 29–52.

(14) Macphee, D.; Folli, A. Photocatalytic Concretes - The Interface Between Photocatalysis and Cement Chemistry. *Cem. Conc. Res.* **2016**, *85*, 48–54.

(15) Serpone, N.; Emeline, A. V.; Ryabchuk, V. K.; Kuznetsov, V. N.; Artem'ev, Y. M.; Horikoshi, S. Why do Hydrogen and Oxygen Yields from Semiconductor-Based Photocatalyzed Water Splitting Remain Disappointingly Low? Intrinsic and Extrinsic Factors Impacting Surface Redox Reactions. *ACS Energy Letters* **2016**, *1*, 931–948.

(16) Protti, S.; Albini, A.; Serpone, N. Photocatalytic Generation of Solar Fuels from the Reduction of H2O and CO2: a Look at the Patent Literature. *Phys. Chem. Chem. Phys.* **2014**, *16*, 19790–19827.

(17) Grätzel, M. Photoelectrochemical Cells. *Nature* **2001**, *414*, 338–344.

(18) Malato, S.; Maldonado, M. I.; Barcelona, D.; Valle, C. Heterogeneous Photocatalytic Hydrogen Generation in a Solar Pilot Plant. *Int. J. Hydrogen Energ.* **2013**, *38*, 12718–12724.

(19) Hopper, H. A.; Le, J.; Cheng, J.; Weller, T.; Marschall, R.; Bloh, J. Z.; Macphee, D. E.; Folli, A.; Mclaughlin, A. C. An Investigation of the Optical Properties and Water Splitting Potential of the Coloured Metallic Perovskites Sr1-xBaxMoO3. *J. Solid State Chem.* **2016**, *234*, 87–92.

(20) Smalley, R. E. Future Global Energy Prosperity: The Terawatt Challenge. *MRS Bulletin* **2005**, *30*, 412–417.

(21) Armaroli, N.; Balzani, V. The Future of Energy Supply: Challenges and Opportunities. *Angew. Chem. Int. Ed.* **2007**, *46*, 52–66.

(22) Lewis, N. S.; Nocera, D. G. Powering the Planet: Chemical Challenges in Solar Energy Utilization. *Proc. Natl. Acad. Sci.* **2006**, *103*, 15729–15735.

(23) Folli, A.; Bloh, J. Z.; Strøm, M.; Pilegaard Madsen, T.; Henriksen, T.; Macphee, D. E. Efficiency of Solar-Light-Driven TiO2 Photocatalysis at Different Latitudes and Seasons. Where and When Does TiO2 Really Work? *J. Phys. Chem. Lett.* **2014**, *5*, 830–832.

(24) Ngaotrakanwiwat, P.; Tatsuma, T.; Saitoh, S.; Ohko, Y.; Fujishima, A. Charge-Discharge Behavior of TiO2-WO3 Photocatalysis Systems with Energy Storage Ability. *Phys. Chem. Chem. Phys.* **2003**, *5*, 3234.

(25) Tatsuma, T.; Saitoh, S.; Ohko, Y.; Fujishima, A. TiO2-WO3 Photoelectrochemical Anticorrosion System with an Energy Storage Ability. *Chem. Mater.* **2001**, *13*, 2838–2842.

(26) Yang, F.; Takahashi, Y.; Sakai, N.; Tatsuma, T. Oxidation of Methanol and Formaldehyde to CO2 by a Photocatalyst with an Energy Storage Ability. *Phys. Chem. Chem. Phys.* **2010**, *12*, 5166–70.

(27) Nguyen, C.-C.; Vu, N.-N.; Do, T.-O. Efficient Hollow Double-Shell Photocatalysts for the Degradation of Organic Pollutants Under Visible Light and in Darkness. *J. Mater. Chem. A* **2016**, *4*, 4413–4419.

(28) Tatsuma, T.; Takeda, S.; Saitoh, S.; Ohko, Y.; Fujishima, A. Bactericidal Effect of an Energy Storage TiO2-WO3 Photocatalyst in Dark. *Electrochem. Comm.* **2003**, *5*, 793–796.

(29) Tatsuma, T.; Saitoh, S.; Ngaotrakanwiwat, P.; Ohko, Y.; Fujishima, A. Energy Storage of TiO2-WO3 Photocatalysis Systems in the Gas Phase. *Langmuir* **2002**, *18*, 7777–7779.

(30) Sotelo-Vazquez, C.; Quesada-Cabrera, R.; Ling, M.; Scanlon, D. O.; Kafizas, A.; Thakur, P. K.; Lee, T.-L.; Taylor, A.; Watson, G. W.; Palgrave, R. G.; Durrant, J. R.; Blackman, C. S.; Parkin, I. P. Evidence and Effect of Photogenerated Charge Transfer for Enhanced Photocatalysis in WO3/TiO2 Heterojunction Films: A Computational and Experimental Study. *Adv. Funct. Mater.* **2017**, *27*, 1605413.

(31) Rietveld, H. M. Line Profiles of Neutron Powder-Diffraction Peaks for Structure Refinenment. *Acta Crystallogr.* **1967**, *22*, 151–152.

(32) Bloh, J. Z.; Folli, A.; Macphee, D. E. Adjusting Nitrogen Doping Level in Titanium Dioxide by Codoping with Tungsten: Properties and Band Structure of the Resulting Materials. *J. Phys. Chem. C* **2014**, *118*, 21281–21292.

(33) Lin, Y. L.; Wang, T. J.; Jin, Y. Surface Characteristics of Hydrous Silica-Coated TiO2 Particles. *Powder Tech.* **2002**, *123*, 194–198.

(34) Iwabuchi, A.; Choo, C.; Tanaka, K. Titania Nanoparticles Prepared with Pulsed Laser Ablation of Rutile Single Crystals in Water. *J. Phys. Chem. B* **2004**, *108*, 10863–10871.

(35) Pouilleau, J.; Devilliers, D.; Groult, H.; Marcus, P. Surface Study of a Titanium-based Ceramic Electrode Material by X-ray Photoelectron Spectroscopy. *J. Mater. Sci.* **1998**, *32*, 5645.

(36) Stefanov, P.; Shipochka, M.; Stefchev, P.; Raicheva, Z.; Lazarova, V.; Spassov, L. XPS Characterization of TiO2 Layers Deposited on Quartz Plates. *J. Phys.: Conf. Ser.* **2008**, *100*, 1–4.

(37) Di Valentin, C.; Finazzi, E.; Pacchioni, G.; Selloni, A.; Livraghi, S.; Paganini, M. C.; Giamello, E. N-doped TiO2: Theory and Experiment. *Chem. Phys.* **2007**, *339*, 44–56.

(38) Momma, K.; Izumi, F. VESTA 3 for Three-Dimensional Visualization of Crystal, Volumetric and Morphology Data. *J. Appl. Cryst.* **2011**, *44*, 1272–1276.

(39) Sato, S.; Nakamura, R.; Abe, S. Visible-Light Sensitization of TiO2 Photocatalysts by Wet-Method N Doping. *Appl. Catal. A* **2005**, *284*, 131–137.

(40) Livraghi, S.; Chierotti, M. R.; Giamello, E.; Magnacca, G.; Paganini, M. C.; Cappelletti, G.; Bianchi, C. L. Nitrogen-Doped Titanium Dioxide Active in Photocatalytic Reactions with Visible Light: A Multi-Technique Characterization of Differently Prepared Materials. *J. Phys. Chem. C* **2008**, *112*, 17244–17252.

(41) Di Valentin, C. D.; Pacchioni, G.; Chiesa, M.; Giamello, E.; Heiz, U.; Nazionale, I.; Cozzi, V. R.; Milano, I.; Ifm, C.; Uni, V.; Nazionale, I.; Giuria, V. P.; Torino, I.; De, I. D. P. NO Monomers on MgO Powders and Thin Films. *J. Phys. Chem. B* **2002**, *106*, 1637–1645.

(42) Livraghi, S.; Paganini, M. C.; Giamello, E.; Selloni, A.; Di Valentin, C.; Pacchioni, G. Origin of Photoactivity of Nitrogen-Doped Titanium Dioxide under Visible Light. *J. Amer. Chem. Soc.* **2006**, *128*, 15666–15671.

(43) Folli, A.; Bloh, J. Z.; Beukes, E. P.; Howe, R. F.; Macphee, D. E. Photogenerated Charge Carriers and Paramagnetic Species in (W,N)- Codoped TiO2 Photocatalysts under Visible-Light Irradiation: An EPR Study. *J. Phys. Chem. C* **2013**, *117*, 22149–22155.

(44) Di Valentin, C.; Pacchioni, G.; Selloni, A.; Livraghi, S.; Giamello, E. Characterization of Paramagnetic Species in N-Doped TiO2 Powders by EPR Spectroscopy and DFT Calculations. *J. Phys. Chem. B* **2005**, *109*, 11414–11419.

(45) Livraghi, S.; Elghniji, K.; Czoska, a. M.; Paganini, M. C.; Giamello, E.; Ksibi, M. Nitrogen-Doped and Nitrogen-Fluorine-Codoped Titanium Dioxide. Nature and Concentration of the Photoactive Species and Their Role in Determining the Photocatalytic Activity under Visible Light. *J. Photochem. Photobiol. A* **2009**, *205*, 93–97.

(46) Folli, A.; Bloh, J. Z.; Walker, R.; Lecaplain, A.; Macphee, D. E. Properties and Photochemistry of Valence-Induced-Ti3+ Enriched (Nb,N)-Codoped Anatase TiO2 Semiconductors. *Phys. Chem. Chem. Phys.* **2015**, *17*, 4849–4853.

(47) Kuba, S.; Heydorn, P.; Grasselli, R. K.; Gates, B. C.; Chec, M.; Kno, H. Redox Properties of Tungstated Zirconia Catalysts : Relevance to the Activation of n-Alkanes. *Phys. Chem. Chem. Phys.* **2001**, *3*, 146–154.

(48) Occhiuzzi, M.; Cordischi, D.; De Rossi, S.; Ferraris, G.; Gazzoli, D.; Valigi, M. Pd-Promoted WOx/ZrO2 Catalysts: Characterization and Catalytic Activity for n-Butane Isomerization. *Appl. Catal. A* **2008**, *351*, 29–35.

(49) Occhiuzzi, M.; Cordischi, D.; Gazzoli, D.; Valigi, M.; Heydorn, P. C. WOx/ZrO2 Catalysts Part 4. Redox Properties as Investigated by Redox Cycles, XPS and EPR. *Appl. Catal. A* **2004**, *269*, 169–177.

(50) Weil, J. A.; Bolton, J. R.; Wertz, J. E. *Electron Paramagnetic Resonance: Elementary Theory and Practical Applications*, 1st ed.; John Wiley & Sons: New York, 1994; p 568.

(51) Wang, X.; Ka, A.; Li, X.; Moniz, S. J. A.; Reardon, P. J. T.; Tang, J.; Parkin, I. P.; Durrant, J. R. Transient Absorption Spectroscopy of Anatase and Rutile: The Impact of Morphology and Phase on Photocatalytic Activity. *J. Phys. Chem. C* **2015**, *119*, 10439–10447.

(52) Gao, R.; Safrany, A.; Rabani, J. Fundamental Reactions in TiO2 Nanocrystallite Aqueous Solutions Studied by Pulse Radiolysis. *Radiat. Phys. Chem.* **2002**, *65*, 599–609.

(53) Mohamed, H. H.; Alomair, N. A.; Bahnemann, D. W. Kinetic and Mechanistic Features on the Reaction of Stored TiO2 Electrons with Hg(II), Pb(II) and Ni(II) in Aqueous Suspension. *Arabian J. Chem.* **2017**, *In press*, 2–9.

(54) Grigioni, I. Development of Photocatalytic Materials for Solar Energy Conversion into Fuels. PhD, University of Milan, 2015.

(55) Kumar, B. V.; Mohanta, D. Probing Spin-Spin and Spin-Lattice Relaxation Through Electron Paramagnetic Resonance Study of Nanoscale WO_{3-x} System. *Mater. Express* **2012**, *2*, 57–63.

(56) Mollet, H. F.; Gerstein, B. C. An EPR Study of W5+ in a Recently Discovered Triclinic Tungsten Bronze, Na0.33WO3. *J. Chem. Phys.* **1974**, *60*, 1440–1446.

(57) Dyson, F. J. Electron Spin Resonance Absorption in Metals. II. Theory of Electron Diffusion and the Skin Effect. *Phys. Rev.* **1955**, *98*, 349–359.

(58) Bloh, J. Z.; Dillert, R.; Bahnemann, D. W. Ruthenium-Modified Zinc Oxide, a Highly Active Vis-Photocatalyst: the Nature and Reactivity of Photoactive Centres. *Phys. Chem. Chem. Phys.* **2014**, *16*, 5833.

(59) Yuan, W.; Li, J.; Wang, L.; Chen, P.; Xie, A.; Shen, Y. Nanocomposite of N-Doped TiO2 Nanorods and Graphene as an Effective Electrocatalyst for the Oxygen Reduction Reaction. *ACS Appl. Mater. Interfaces* **2014**, *6*, 21978–21985.

(60) Seifitokaldani, A. Oxygen Reduction Reaction (ORR) on Mixed Oxy-Nitride Non-Noble Catalyst: Ab-Initio Simulation, Elaboration and Characterization. Ph.D. thesis, École Polytechnique de Montréal, 2014.

(61) Patzsch, J.; Folli, A.; Macphee, D. E.; Bloh, J. Z. On the Underlying Mechanisms of the Low Observed Nitrate Selectivity in Photocatalytic NOx Abatement and the Importance of the Oxygen Reduction Reaction. *Phys. Chem. Chem. Phys.* **2017**, *19*, 32678–32686.

(62) Devahasdin, S.; Fan, C. J.; Li, K.; Chen, D. H. TiO2 Photocatalytic Oxidation of Nitric Oxide: Transient Behavior and Reaction Kinetics. *J. Photochem. Photobiol. A* **2003**, *156*, 161–170.

(63) Folli, A.; Campbell, S. B.; Anderson, J. A.; Macphee, D. E. Role of TiO2 Surface Hydration on NO Oxidation Photo-Activity. *J. Photochem. Photobiol. A* **2011**, *220*, 85–93.

(64) Ohko, Y.; Nakamura, Y.; Negishi, N.; Matsuzawa, S.; Takeuchi, K. Photocatalytic Oxidation of Nitrogen Monoxide Using TiO2 Thin Films under Continuous UV Light Illumination. *J. Photochem. Photobiol. A* **2009**, *205*, 28–33.

(65) Larson, A. C.; Von Dreele, R. B. *General Structure Analysis System (GSAS) - Technical Report No. LAUR86-748*; 2004.

(66) Stoll, S.; Schweiger, A. EasySpin, a Comprehensive Software Package for Spectral Simulation and Analysis in EPR. *J. Magn. Reson.* **2006**, *178*, 42–55.

(67) Parker, C. A. A New Sensitive Chemical Actinometer. I. Some Trials with Potassium Ferrioxalate. *Proc. R. Soc. Lond. A* **1953**, *220*, 104–116.

(68) Hatchard, C. G.; Parker, C. A. A New Sensitive Chemical Actinometer. II. Potassium Ferrioxalate as a Standard Chemical Actinometer. *Proc. R. Soc. Lond. A* **1956**, *235*, 518–536.

(69) Kuhn, H.; Braslavsky, S.; Schmidt, R. *Chemical Actinometry*; 2005; pp 1–47.

Table of Content Graphics (TOC)

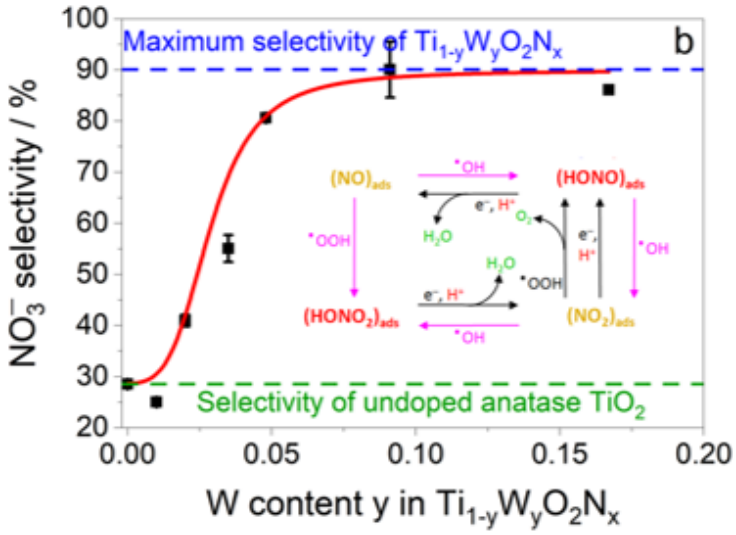

SUPPORTING INFORMATION

Improving the selectivity of photocatalytic NOx abatement through improved O_2 reduction pathways using $Ti_{0.909}W_{0.091}O_2N_x$ semiconductor nanoparticles: from characterisation to photocatalytic performance

Andrea Folli,*,† Jonathan Z. Bloh,‡ Katherine Armstrong,† Emma Richards,† Damien M. Murphy,† Li Lu,¶ Christopher J. Kiely,¶,† David J. Morgan,† Ronald I. Smith,§ Abbie C. Mclaughlin,‖ and Donald E. Macphee‖

†*School of Chemistry, Cardiff University, Main Building, Park Place, Cardiff CF10 3AT, UK.*

‡*DECHEMA Research Institute, Theodor-Heuss-Allee 25, Frankfurt am Main 60468, Germany.*

¶*Department of Materials Science and Engineering, Lehigh University, Whitaker Laboratory, 5 East Packer Ave, Bethlehem, PA 18015, USA.*

§*ISIS Neutron and Muon Source, STFC Rutherford Appleton Laboratory, Harwell Campus, Didcot OX11 0QX, UK.*

‖*Department of Chemistry, University of Aberdeen, Meston Building, Meston Walk, Aberdeen AB24 3UE, UK.*

E-mail: follia@cardiff.ac.uk

Contents

1 X-band CW EPR spectra under irradiation

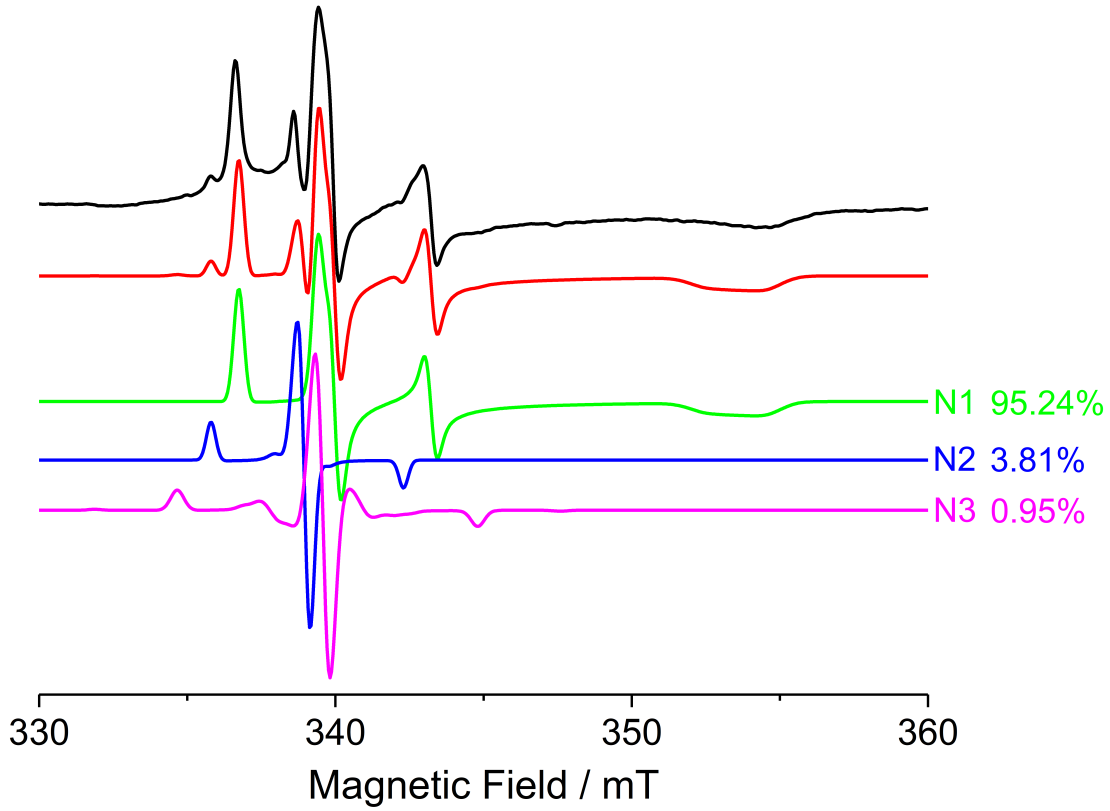

Figure S1: Experimental (black) and simulated (red) X-band CW EPR spectra of the $Ti_{0.909}W_{0.091}O_2N_x$ nanoparticles under irradiation with a 455 nm LED light source, measured at 50 K around the free spin region. The simulated spectrum is deconvoluted into its three components N1 (green), N2 (blue) and N3 (magenta). The relative spectral contributions are also reported in the Figure. The experimental spectrum was recorded at 100 kHz field modulation frequency; 0.2 mT field modulation amplitude; 2 µW microwave power and 72 dB receiver gain.

.

.

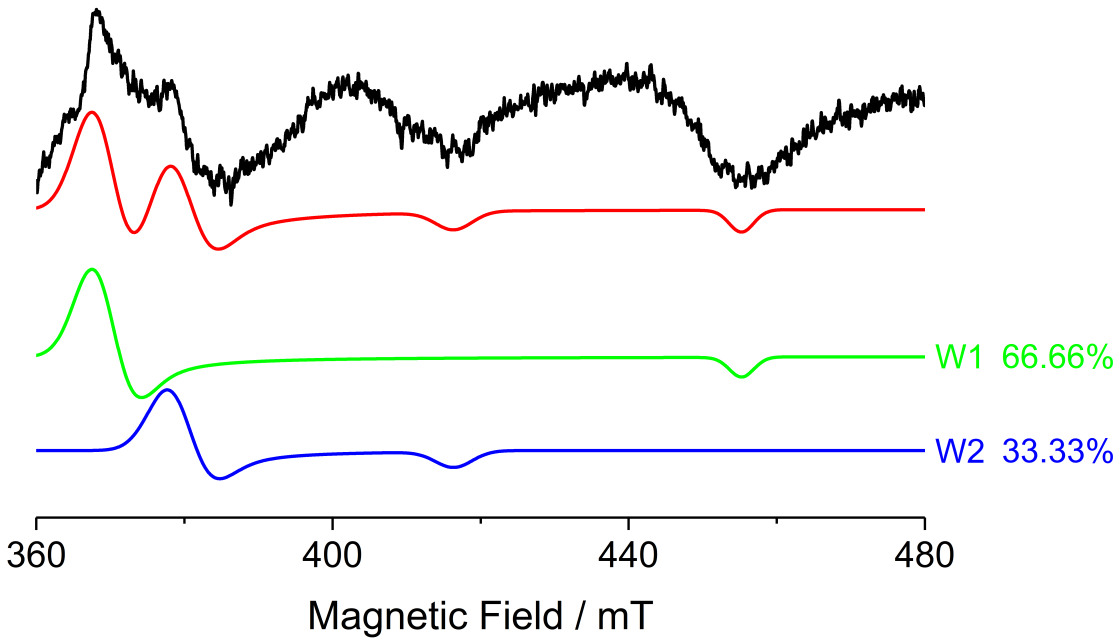

Figure S2: Experimental (black) and simulated (red) X-band CW EPR spectra of the $Ti_{0.909}W_{0.091}O_2N_x$ nanoparticles under irradiation with a 455 nm LED light source, measured at 50 K at high fields. The simulated spectrum is deconvoluted into its two components W1 (green), W2 (blue). The relative spectral contributions are also reported in the Figure. The experimental spectrum was recorded at 100 kHz field modulation frequency; 0.2 mT field modulation amplitude; 2 µW microwave power and 72 dB receiver gain.

2 Dyson line simulation and analysis

The EPR spectrum at low fields reported in Figure 11 of the main manuscript was simulated using a Dyson function with three parameters:[1]

$$P_D \propto \left[\frac{\Delta B + \alpha(B - B_0)}{4(B - B_0)^2 + \Delta B^2} + \frac{\Delta B + \alpha(B + B_0)}{4(B + B_0)^2 + \Delta B^2} \right] \tag{S1}$$

that was differentiated with respect to the magnetic field B to obtain the signal amplitude s.a. of the derivative of resonance (first harmonic):

$$s.a. = \frac{dP_D}{dB} \tag{S2}$$

In equation S1, α, also called asymmetry parameter, represents the ratio of signal amplitude of the left peak A to the right peak B in the derivative of resonance; ΔB is the Dyson linewidth and B_0 is the Dyson line position in mT. Simulation was performed as best fit of Equation S2 to the experimental spectrum in Figure 11, from which the optimised parameters (reported in Figure 11) α, ΔB and B_0 were derived. The fitting was perfomed using a non-linear least square method based on the Levenberg-Marquardt algorithm, with: function tolerance 10^{-6}, maximum number of iterations 400, maximum function evalutations 1500.

References

(1) Popovych, V.; Bester, M.; Stefaniuk, I.; Kuzma, M. Dyson Line and Modified Dyson Line in the EPR Measurements. *Nukleonika* **2015**, *60*, 385–388.